Available online at www.sciencedirect.com
ScienceDirect
Comput. Methods Appl. Mech. Engrg. 390 (2022) 114438
Computer methods in applied mechanics and engineering
www.elsevier.com/locate/cma

Topological derivative-based topology optimization of incompressible structures using mixed formulations

Inocencio Castañar[a], Joan Baiges[a,*], Ramon Codina[a,b], Henning Venghaus[b]

[a] *Universitat Politècnica de Catalunya, Barcelona Tech, Jordi Girona 1-3, Edifici C1, 08034 Barcelona, Spain*
[b] *Centre Internacional de Mètodes Numèrics en Enginyeria (CIMNE), Edifici C1, Campus Nord UPC, Gran Capitán S/N, 08034 Barcelona, Spain*

Received 16 June 2021; received in revised form 22 November 2021; accepted 5 December 2021
Available online 1 January 2022

Abstract

In this work an algorithm for topological optimization, based on the topological derivative concept, is proposed for both nearly and fully incompressible materials. In order to deal with such materials, a new decomposition of the Polarization tensor is proposed in terms of its deviatoric and volumetric components. Mixed formulations applied in the context of linear elasticity do not only allow to deal with incompressible material behavior but also to obtain a higher accuracy in the computation of stresses. The system is stabilized by means of the Variational Multiscale method based on the decomposition of the unknowns into resolvable and subgrid scales in order to prevent fluctuations. Several numerical examples are presented and discussed to assess the robustness of the proposed formulation and its applicability to Topology Optimization problems for incompressible elastic solids.

Keywords: Topology optimization; Topological derivative; Incompressible elasticity; Mixed interpolations; Stabilization methods

1. Introduction

Structural topology optimization aims to find the optimal layout of material within a design domain for a given set of boundary conditions such that the resulting material distribution meets a set of performance targets [1]. Several types of topology optimization methodologies exist, such as density-based methods which include the popular SIMP technique [2], hard-kill methods [3] and boundary variation methods [4], among others [5]. A relatively new approach for this kind of problem is based on the topological derivative concept [6]. This derivative measures the sensitivity of a given shape functional with respect to an infinitesimal singular domain perturbation and it has become a very powerful tool due to the fact that it can be used as a steepest-descent direction in an optimization process [7–10].

An incompressible material is understood as one which keeps its volume constant throughout a motion. In many cases, this is a common idealization and accepted assumption, often invoked in continuum and computational mechanics. Numerous polymeric materials can sustain finite strains without noticeable volume changes. Furthermore, many biological materials and several types of soils can be modeled as nearly or fully incompressible [11].

* Corresponding author.
E-mail addresses: icastanar@cimne.upc.edu (I. Castañar), jbaiges@cimne.upc.edu (J. Baiges), ramon.codina@upc.edu (R. Codina), hvenghaus@cimne.upc.edu (H. Venghaus).

https://doi.org/10.1016/j.cma.2021.114438
0045-7825/

In small strain solid mechanics problems, standard irreducible low order finite elements are typically preferred [12]. *Standard irreducible* means that only the displacement field is considered as the primary unknown of the problem and all other fields, such as stress and strain fields, are obtained a posteriori. Unfortunately, this approach performs poorly in nearly and fully incompressible scenarios: volumetric and shear locking, pressure fluctuations and poor performance in bending dominated situations are some of the effects that can be observed [13].

To overcome these problems an approach which originated in fluid mechanics can be adapted. When considering a static, incompressible, infinitesimal strain case of the solid mechanics problem, we obtain an elliptic problem which is identical to the formulation of the Stokes problem in fluid mechanics [14,15]. It is therefore reasonable to convey the mixed velocity/pressure approach, used in fluid mechanics to the solid mechanics problem — becoming the mixed displacement/pressure approach [16]. This approach led to the extension of different implementations in the field of fluid mechanics to the solid mechanics area. See for instance [17–20], a set of works where the incompressible nonlinear material problem is stabilized using the variational multiscale method. Note that in the cited papers the orthogonal subscales method [21,22] is used, which is a variant of the original stabilization method proposed in [23]. These works, in which both strain/displacement as well as stress/displacement pairs are used as primary variables, demonstrate the good performance of mixed finite elements in solid mechanics. By using more than one primary unknown, the number of unknowns per node is considerably increased – especially when considering stresses or strains – but they also increase the accuracy notably. Furthermore, in [24] the idea of using displacement/pressure/stress or displacement/pressure/strain formulations, proposed in [25], was tested and seen to be very effective when solving incompressible cases in which also accurate results for the stress and strain field are required.

To the best of our knowledge, only few studies exist which face the topology optimization problem of incompressible materials. In [26,27], mixed formulations with very specific interpolation schemes for the elements are applied with a class of SIMP interpolations [28] for both the bulk and shear modulus. The subsequent optimization problem is solved using the Method of Moving Asymptotes [29]. Further, [30] proposes the scaled boundary finite element method (SBFEM) formulation to avoid the inf–sup condition for the mixed displacement/pressure problem and applies the moving iso-surface threshold (MIST) method to solve the topology optimization problem. Finally, in [31] a density-based topology optimization problem is proposed for several material interpolations and by also using the mixed displacement/pressure formulation for nearly incompressible materials.

In the present work, we favor using the topological derivative concept in combination with a level-set method to address the topology optimization problem. However, in the context of structural topology design, the topological derivative has been only used as a descent direction utilizing the classical displacement-based formulation [32]. This approach is therefore limited to compressible materials. Considering nearly and fully incompressible material behavior, both the formulation and the topological derivative expression become singular. We overcome this problem by introducing the deviatoric/volumetric split, as presented in [24], thus obtaining a mixed formulation. Following this approach, the present work proposes a new expression for the split topological derivative which allows us to compute the correct topological derivative for incompressible materials. Together with a level-set method, this approach is used to obtain optimal designs.

This paper is organized as follows. In Section 2 the mixed displacement/pressure ($\mathbf{u}/p$) and the displacement/pressure/deviatoric strain ($\mathbf{u}/p/\mathbf{e}$) finite element formulations for linear elasticity are summarized and the sub-grid scale approach is outlined. In Section 3 a new topological derivative expression is defined through the volumetric–deviatoric decomposition of the Polarization tensor. Next, in Section 4, the proposed iterative topology optimization algorithm is presented. In Section 5 several numerical examples are presented and discussed to assess the present algorithm and to validate its performance for nearly and fully incompressible materials. Finally, in Section 6 some conclusions of the proposed topology optimization formulations are drawn.

2. Mixed formulations in linear elasticity

2.1. The continuum problem statement

In this work, the equations of motion are presented under the infinitesimal strain assumption. Let Ω be an open, bounded and polyhedral domain of $\mathbb{R}^d$, where d is the number of spacial dimensions. Any point of the body is labeled with the vector $\mathbf{x}$. The boundary of the domain is denoted as $\Gamma := \partial\Omega$ and is split into a Dirichlet boundary

Γ_D, where the prescribed displacements are specified, and a Neumann boundary Γ_N, where prescribed tractions are applied. The types of boundaries do not intersect, $\Gamma_D \cap \Gamma_N = \emptyset$ and together cover the whole boundary, $\Gamma_D \cup \Gamma_N = \Gamma$.

The continuum mechanical problem of linear elasticity is defined by the following system of equations

$$-\nabla \cdot \boldsymbol{\sigma} = \rho \mathbf{b} \quad \text{in } \Omega, \tag{1}$$

$$\boldsymbol{\sigma} = \mathbb{C} : \boldsymbol{\varepsilon} \quad \text{in } \Omega, \tag{2}$$

$$\boldsymbol{\varepsilon} = \nabla^{\mathrm{s}} \mathbf{u} \quad \text{in } \Omega, \tag{3}$$

where $\mathbf{u}$ is the displacement field, $\boldsymbol{\sigma}$ the stress field and $\boldsymbol{\varepsilon}$ the strain field. Eq. (1) is the balance of momentum equation, where $\rho \mathbf{b}$ represents the external load per unit of volume and $\nabla \cdot (\cdot)$ is the divergence operator. Eq. (2) is the constitutive equation for linear elasticity, where $\mathbb{C}$ is the 4th order constitutive tensor for isotropic materials defined as

$$\mathbb{C} = 2\mu \mathbb{I} + \lambda \mathbf{I} \otimes \mathbf{I}. \tag{4}$$

Here, $\mathbb{I}$ and $\mathbf{I}$ are the 4th rank and the 2nd rank identity tensors, respectively, and λ and μ are Lamé's parameters. In the plane stress assumption they are expressed as

$$\lambda = \frac{\nu E}{1-\nu^2} \quad \text{and} \quad \mu = \frac{E}{2(1+\nu)}, \tag{5}$$

while in both 3D and plane strain they are defined as

$$\lambda = \frac{\nu E}{(1+\nu)(1-2\nu)} \quad \text{and} \quad \mu = \frac{E}{2(1+\nu)}. \tag{6}$$

Here E is the Young modulus and ν the Poisson ratio. Finally, Eq. (3) is the kinematic equation which relates the strain field with displacements, where $\nabla^s(\cdot) = \frac{1}{2}\left\{\nabla(\cdot) + \nabla^T(\cdot)\right\}$ denotes the symmetric gradient operator and $\nabla(\cdot)$ is the gradient operator.

The classical irreducible displacement-based formulation is obtained by substituting Eqs. (2)–(3) into Eq. (1). The result is known as Navier's equation

$$-\nabla \cdot \left\{\mathbb{C} : \nabla^{\mathrm{s}} \mathbf{u}\right\} = \rho \mathbf{b} \quad \text{in } \Omega, \tag{7}$$

which is written in terms of the displacement field only.

2.2. The volumetric/deviatoric split

The objective of this subsection is the split of both the constitutive and the kinematic equation into their volumetric and deviatoric parts. The volumetric/deviatoric split is the starting point to develop a formulation able to tackle the incompressible limit.

2.2.1. Volumetric and deviatoric operators

First of all, let us define the volumetric and deviatoric 4th order tensors $\mathbb{V}$ and $\mathbb{D}$ as

$$\mathbb{V} = \frac{1}{3}\mathbf{I} \otimes \mathbf{I}, \tag{8}$$

$$\mathbb{D} = \mathbb{I} - \frac{1}{3}\mathbf{I} \otimes \mathbf{I}, \tag{9}$$

$$\mathbb{I} = \mathbb{D} + \mathbb{V}. \tag{10}$$

Using the operators $\mathbb{V}$ and $\mathbb{D}$, it is possible to extract the spherical and the deviatoric parts of generic 2nd and 4th order tensors.

2.2.2. Split of stress and strain tensors

Particularly, when applied to the stress tensor $\boldsymbol{\sigma}$ the result is

$$\mathbb{V} : \boldsymbol{\sigma} = \left\{\frac{1}{3}\mathbf{I} \otimes \mathbf{I}\right\} : \boldsymbol{\sigma} = \frac{1}{3}\mathrm{tr}(\boldsymbol{\sigma})\mathbf{I} := -p\mathbf{I}, \tag{11}$$

where p is the pressure, taken as positive in compression regime and

$$\mathbb{D} : \boldsymbol{\sigma} = \left\{ \mathbb{I} - \frac{1}{3}\mathbf{I} \otimes \mathbf{I} \right\} : \boldsymbol{\sigma} = \boldsymbol{\sigma} + p\mathbf{I} = \mathbf{s}, \tag{12}$$

where $\mathbf{s}$ are the deviatoric stresses. Adding the volumetric and the deviatoric components, the Cauchy stress tensor is rebuilt as

$$\boldsymbol{\sigma} = \mathbf{s} - p\mathbf{I}. \tag{13}$$

In a similar way, it is possible to split the strain tensor $\boldsymbol{\varepsilon}$, as

$$\mathbb{V} : \boldsymbol{\varepsilon} = \left\{ \frac{1}{3}\mathbf{I} \otimes \mathbf{I} \right\} : \boldsymbol{\varepsilon} = \frac{1}{3}\mathrm{tr}(\boldsymbol{\varepsilon})\mathbf{I} := \frac{1}{3}e^{\mathrm{vol}}\mathbf{I}, \tag{14}$$

where e^{vol} is the volumetric deformation and

$$\mathbb{D} : \boldsymbol{\varepsilon} = \left\{ \mathbb{I} - \frac{1}{3}\mathbf{I} \otimes \mathbf{I} \right\} : \boldsymbol{\varepsilon} = \boldsymbol{\varepsilon} - \frac{1}{3}e^{\mathrm{vol}}\mathbf{I} = \mathbf{e}, \tag{15}$$

where $\mathbf{e}$ are the deviatoric strains which account for the distortions.

2.2.3. Split of the kinematic equation

Applying the volumetric/deviatoric operators, Eq. (3) is split as

$$e^{\mathrm{vol}} = \nabla \cdot \mathbf{u}, \tag{16}$$

$$\mathbf{e} = \mathbb{D} : \nabla^{\mathrm{s}}\mathbf{u}. \tag{17}$$

Adding the volumetric and the deviatoric components, the kinematic equation is rebuilt as

$$\boldsymbol{\varepsilon} = \frac{1}{3}e^{\mathrm{vol}}\mathbf{I} + \mathbf{e} = \frac{1}{3}(\nabla \cdot \mathbf{u})\mathbf{I} + \mathbb{D} : \nabla^{\mathrm{s}}\mathbf{u}. \tag{18}$$

2.2.4. Split of the constitutive equation

Let us assume that the constitutive relationship between stresses and strains can be expressed utilizing the constitutive Eq. (2). Hence, the volumetric and the deviatoric parts of the constitutive tensor $\mathbb{C}^{\mathrm{vol}}$ and $\mathbb{C}^{\mathrm{dev}}$ are obtained as

$$\mathbb{C}^{\mathrm{vol}} = \mathbb{V} : \mathbb{C} = (\lambda + \frac{2\mu}{3})\mathbf{I} \otimes \mathbf{I} := \kappa\mathbf{I} \otimes \mathbf{I}, \tag{19}$$

$$\mathbb{C}^{\mathrm{dev}} = \mathbb{D} : \mathbb{C} = 2\mu \left\{ \mathbb{I} - \frac{1}{3}\mathbf{I} \otimes \mathbf{I} \right\}, \tag{20}$$

$$\mathbb{C} = \mathbb{C}^{\mathrm{vol}} + \mathbb{C}^{\mathrm{dev}}, \tag{21}$$

where κ is the bulk modulus of the material. Introducing the split of stresses and strains, the constitutive relationship in Eq. (2) can be written as

$$\{\mathbf{s} - p\mathbf{I}\} = \left\{ \mathbb{C}^{\mathrm{vol}} + \mathbb{C}^{\mathrm{dev}} \right\} : \left\{ \frac{1}{3}(\nabla \cdot \mathbf{u})\mathbf{I} + \mathbb{D} : \nabla^{\mathrm{s}}\mathbf{u} \right\} \tag{22}$$

By taking into account that the contraction between volumetric and deviatoric tensors is identically null, Eq. (22) is split into two equations

$$p = -\kappa\nabla \cdot \mathbf{u}, \tag{23}$$

$$\mathbf{s} = \mathbb{C}^{\mathrm{dev}} : \boldsymbol{\varepsilon} = \mathbb{C}^{\mathrm{dev}} : \mathbf{e}, \tag{24}$$

which are the volumetric and the deviatoric counterparts of the original constitutive equation.

2.3. The $\mathbf{u}/p$ two-field formulation

In this section, the well-known mixed $\mathbf{u}/p$ formulation is introduced in order to deal with nearly and fully incompressible scenarios. In the presented formulation the displacement and pressure fields $\mathbf{u}$ and p are used as independent variables. Hence, the governing equations of the problem are rewritten as

$$-\nabla\cdot\mathbf{s}+\nabla p=\rho\mathbf{b} \qquad \text{in } \Omega, \tag{25}$$

$$\mathbf{s}=\mathbb{C}^{\text{dev}}:\nabla^{\text{s}}\mathbf{u} \qquad \text{in } \Omega, \tag{26}$$

$$\nabla\cdot\mathbf{u}+\frac{p}{\kappa}=0 \qquad \text{in } \Omega. \tag{27}$$

Eq. (25) allows us to formulate the linear momentum equation in terms of both displacements $\mathbf{u}$ and pressure p, where the stress tensor decomposition (13) has been introduced into the momentum equation. Furthermore, the constitutive law which relates deviatoric stresses with displacements (26) allows us to introduce the displacement field in the balance equation (25). Finally, Eq. (27) is in charge of both providing the constitutive equation for the pressure and imposing the incompressibility constraint.

Remark 2.1. Let us recall that in the incompressible limit $\kappa\to\infty$, and Eq. (27) will reduce automatically to

$$\nabla\cdot\mathbf{u}=0, \tag{28}$$

which is the incompressibility condition for infinitesimal strain theory.

2.3.1. Governing equations

To complete this section, we introduce the mixed $\mathbf{u}/p$ problem, which consists in finding both a displacement $\mathbf{u}$ and a pressure p such that

$$-\nabla\cdot\left\{\mathbb{C}^{\text{dev}}:\nabla^{\text{s}}\mathbf{u}\right\}+\nabla p=\rho\mathbf{b} \qquad \text{in } \Omega, \tag{29}$$

$$\nabla\cdot\mathbf{u}+\frac{p}{\kappa}=0 \qquad \text{in } \Omega. \tag{30}$$

The governing equations must be supplied with a set of boundary conditions

$$\mathbf{u}=\mathbf{u}_D \qquad \text{on } \Gamma_D, \tag{31}$$

$$\boldsymbol{\sigma}\mathbf{n}\overset{(13)}{=}\mathbf{s}\mathbf{n}-p\mathbf{n}=\mathbf{t} \qquad \text{on } \Gamma_N, \tag{32}$$

where $\mathbf{n}$ is the geometric unit outward normal vector on the boundary Γ. To simplify the exposition, we will consider $\mathbf{u}_D=0$ in the following.

2.3.2. Variational form of the problem

We shall use the symbol $(\cdot,\cdot)_\omega$ to refer to the $L^2(\omega)$ inner product and $\langle\cdot,\cdot\rangle_\omega$ to refer to the integral of the product of two functions in a domain ω, not necessarily in $L^2(\omega)$. The subscript is omitted when $\omega=\Omega$.

Let $\mathbb{V}^d=\left[H^1(\Omega)\right]^d$ and $\mathbb{Q}=L^2(\Omega)$ be, respectively, the proper functional spaces where displacement and pressure solutions are well-defined. We denote by $\mathbb{V}_0^d$ functions in $\mathbb{V}^d$ which vanish in the Dirichlet boundary Γ_D. We shall be interested also in the spaces $\mathbb{W}:=\mathbb{V}\times\mathbb{Q}$, $\mathbb{W}_0:=\mathbb{V}_0\times\mathbb{Q}$. The variational statement of the problem is derived by testing the system presented in Eqs. (29)–(30) against arbitrary test functions $\mathbf{V}:=[\mathbf{v},q]^T$, $\mathbf{v}\in\mathbb{V}_0^d$ and $q\in\mathbb{Q}$. The weak form of the problem reads: find $\mathbf{U}:=[\mathbf{u},p]^T\in\mathbb{W}_0$ such that

$$\mathcal{A}(\mathbf{U},\mathbf{V})=\mathcal{F}(\mathbf{V}) \quad \forall\mathbf{V}\in\mathbb{W}_0, \tag{33}$$

where $\mathcal{A}(\mathbf{U},\mathbf{V})$ is a bilinear form defined on $\mathbb{W}_0\times\mathbb{W}_0$ as

$$\mathcal{A}(\mathbf{U},\mathbf{V}):=\left(\nabla^s\mathbf{v},\mathbb{C}^{\text{dev}}:\nabla^s\mathbf{u}\right)-(\nabla\cdot\mathbf{v},p)+(q,\nabla\cdot\mathbf{u})+\left(q,\frac{1}{\kappa}p\right). \tag{34}$$

$\mathcal{F}(\mathbf{V})$ is a linear form defined on $\mathbb{W}_0$ as

$$\mathcal{F}(\mathbf{V}):=\langle\mathbf{v},\rho\mathbf{b}\rangle+\langle\mathbf{v},\mathbf{t}\rangle_{\Gamma_N}. \tag{35}$$

As usual, integration by parts has been used in order to decrease the continuity requirements of unknowns $\mathbf{u}$ and p and the traction vector $\mathbf{t}$ has been identified.

2.3.3. Galerkin Spatial discretization

The standard Galerkin approximation of this abstract variational problem is now straightforward. Let $\mathcal{P}_h$ denote a finite element partition of the domain Ω. The diameter of an element domain $K \in \mathcal{P}_h$ is denoted by h_K and the diameter on the finite element partition by $h = \max\{h_K | K \in \mathcal{P}_h\}$. We can now construct conforming finite element spaces $\mathbb{V}_h \subset \mathbb{V}$, $\mathbb{Q}_h \subset \mathbb{Q}$ and $\mathbb{W}_h = \mathbb{V}_h \times \mathbb{Q}_h$ in the usual manner, as well as the corresponding subspaces $\mathbb{V}_{h,0} \subset \mathbb{V}_0$ and $\mathbb{W}_{h,0} = \mathbb{V}_{h,0} \times \mathbb{Q}_h$, $\mathbb{V}_{h,0}$ being made with functions that vanish on the Dirichlet boundary.

The Galerkin discrete version of problem (33) is: find $\mathbf{U}_h \in \mathbb{W}_{h,0}$ such that

$$\mathcal{A}(\mathbf{U}_h, \mathbf{V}_h) = \mathcal{F}(\mathbf{V}_h) \quad \forall \mathbf{V}_h \in \mathbb{W}_{h,0}. \tag{36}$$

The well posedness of this problem relies on an inf–sup condition [33]. This condition is necessary and sufficient for the existence and uniqueness of the solution to the discrete saddle-point problem. Convenient displacement–pressure interpolations, such as equal interpolation, turn out to violate the inf–sup condition. This is why the so-called stabilized formulations have been proposed to approximate this kind of problems. The main idea is to replace (33) by another discrete variational problem in which the bilinear form $\mathcal{A}(\cdot,\cdot)$ is enhanced so that it has improved stability properties. In order to overcome the instabilities previously discussed, we propose to use the stabilization technique described in next section.

Remark 2.2. In principle, we have posed no restrictions on the choice of the finite element spaces. However, let us analyze the numerical stability of problem (36). If we take $\mathbf{V}_h = \mathbf{U}_h$, it is found that

$$\mathcal{A}(\mathbf{U}_h, \mathbf{U}_h) = \left(\nabla^s \mathbf{u}_h, \mathbb{C}^{\text{dev}} : \nabla^s \mathbf{u}_h\right) + \left(p_h, \frac{1}{\kappa} p_h\right) \geq c\|\mathbb{D} : \nabla^s \mathbf{u}\|^2 + \frac{1}{\kappa}\|p_h\|^2. \tag{37}$$

where $\|\cdot\|$ is the $L^2(\Omega)$ norm . It is seen from Eq. (37) that $\mathcal{A}(\cdot,\cdot)$ is not coercive in $\mathbb{W}_h$ when $\kappa \to \infty$, the pressure being out of control. Hence, in the nearly and fully incompressible cases the inf–sup condition is not satisfied.

2.3.4. Stabilized $\mathbf{u}/p$ finite element formulation

The stabilized finite element method we propose to use in the following is based on the variational multiscale concept (VMS) [23,34]. Let $\mathbb{W} = \mathbb{W}_h \oplus \tilde{\mathbb{W}}$, where $\tilde{\mathbb{W}}$ is any space to complete $\mathbb{W}_h$ in $\mathbb{W}$. $\tilde{\mathbb{W}}$ will be approximated by a finite-dimensional space despite the fact that it is infinite-dimensional. The elements of this space are denoted by $\tilde{\mathbf{U}} \equiv \left[\tilde{\mathbf{u}}, \tilde{p}\right]^T$ and they are called subscales. Likewise, let $\mathbb{W}_0 = \mathbb{W}_{h,0} \oplus \tilde{\mathbb{W}}_0$.

Taking into account that $\mathcal{A}(\cdot,\cdot)$ is a bilinear form, the continuous problem (33) is equivalent to find $\mathbf{U} \in \mathbb{W}_{h,0}$ and $\tilde{\mathbf{U}} \in \tilde{\mathbb{W}}_0$ such that

$$\mathcal{A}(\mathbf{U}_h, \mathbf{V}_h) + \mathcal{A}\left(\tilde{\mathbf{U}}, \mathbf{V}_h\right) = \mathcal{F}(\mathbf{V}_h) \qquad \forall \mathbf{V}_h \in \mathbb{W}_{h,0}, \tag{38}$$

$$\mathcal{A}\left(\mathbf{U}_h, \tilde{\mathbf{V}}\right) + \mathcal{A}\left(\tilde{\mathbf{U}}, \tilde{\mathbf{V}}\right) = \mathcal{F}\left(\tilde{\mathbf{V}}\right) \qquad \forall \tilde{\mathbf{V}} \in \tilde{\mathbb{W}}_0, \tag{39}$$

where Eq. (38) is called the finite element scale equation and Eq. (39) is called the subgrid scale equation.

The main idea behind any stabilized finite element method derived from the VMS framework is to obtain an expression for the subscales from the subgrid scale Eq. (39). This is done to complement our finite element scale Eq. (38) to ensure consistency of the stabilized mixed formulation so that the discrete solution converges to the continuous solution on mesh refinement. We assume the subscales to behave as bubble functions, which means that they vanish across inter-element boundaries. Therefore, the sub-grid scale is expressed in terms of the residual of the projected (Galerkin) counterpart of Eqs. (29)–(30) to obtain

$$\tilde{\mathbf{u}} \approx \tau_{\mathbf{u}} \tilde{\Pi} \left(\nabla \cdot \mathbf{s}_h - \nabla p_h - \rho \mathbf{b}\right), \tag{40}$$

$$\tilde{p} \approx \tau_p \tilde{\Pi} \left(-\nabla \cdot \mathbf{u}_h - \frac{1}{\kappa} p_h\right), \tag{41}$$

where $\tilde{\Pi}$ is the $L^2(\Omega)$ projection onto the space of subscales and $\tau_{\mathbf{u}}$ and τ_p are coefficients coming from a Fourier analysis of the problem for the subscales. In this work, we use the stabilization parameters proposed in [18] for linear elastic cases

$$\tau_{\mathbf{u}} = c_1 \frac{h_K^2}{2\mu} \quad \text{and} \quad \tau_p = 2c_2 \left(\frac{1}{\mu} + \frac{2}{3\kappa}\right)^{-1}, \tag{42}$$

where c_1 and c_2 are algorithmic parameters which must be determined.

Introducing the approximate fields (40)–(41) into the finite element scale problem (38), the VMS stabilized formulation of the problem is obtained as

$$\begin{aligned}\mathcal{A}\left(\mathbf{U}_h, \mathbf{V}_h\right) + \sum_K \tau_{\mathbf{u}} \left\langle -\nabla q_h, \tilde{\Pi}\left(\nabla \cdot \mathbf{s}_h - \nabla p_h - \rho \mathbf{b}\right)\right\rangle_K \\ + \sum_K \tau_p \left\langle -\nabla \cdot \boldsymbol{v} + \frac{1}{\kappa} q_h, \tilde{\Pi}\left(-\nabla \cdot \mathbf{u}_h - \frac{1}{\kappa} p_h\right)\right\rangle_K = \mathcal{F}\left(\mathbf{V}_h\right) \quad \forall \mathbf{V}_h \in \mathbb{W}_{h,0}.\end{aligned} \tag{43}$$

There exist several stabilization methods coming from the VMS technique depending on the selection of the projection onto the subscales space. In this work, two different options are considered:

(1) We take the projection onto the subscales space as the identity when applied to the residual. This approach is called Algebraic SubGrid Scales (ASGS), see [15] for further details.
(2) In [21] it is argued that the natural approximation for the unknown subgrid space is to take it orthogonal to the finite element space. This approach is called Orthogonal Subgrid Scales (OSS).

Remark 2.3. A key property of the OSS stabilization is that thanks to the orthogonal projection onto the finite element space, we keep the consistency of the formulation in a weak sense despite including just the minimum number of terms to stabilize the solution if $\tilde{\Pi}$ does not include Dirichlet-type boundary conditions (see [34]). For this specific formulation, we can reduce the stabilization terms to solely $\sum_K \tau_{\mathbf{u}} \left\langle \nabla q_h, \tilde{\Pi}\left(\nabla p_h\right)\right\rangle$.

2.4. The $\mathbf{u}/p/\mathbf{e}$ three-field formulation

In this section we present the mixed three field formulation used to deal with the solid mechanics problem. The methodology was originally developed in [25] to deal with the Stokes problem in fluid mechanics, and extended to solid mechanics in [24] by considering the deviatoric stresses as an additional unknown of the problem. More recently, in [35], the formulation was adapted so that the main unknowns are displacements, pressure and deviatoric strains, instead deviatoric stresses, which is the approach we follow in this work. The displacement field $\mathbf{u}$, together with the deviatoric component of the strains $\mathbf{e}$, as well as the pressure field p are taken as primary unknowns of the problem. The objective is the definition of a general framework, which includes the well-known mixed $\mathbf{u}/p$ formulation. Therefore we are capable of correctly describing nearly and fully incompressible material behavior. Adding the deviatoric strains as unknowns allows us to obtain a high degree of accuracy for the strain field but also for the stress field. The governing equations of the problem are rewritten as

$$-\nabla \cdot \mathbf{s} + \nabla p = \rho \mathbf{b} \qquad \text{in } \Omega, \tag{44}$$

$$\mathbf{s} = \mathbb{C}^{\text{dev}} : \mathbf{e} \qquad \text{in } \Omega, \tag{45}$$

$$\nabla \cdot \mathbf{u} + \frac{p}{\kappa} = 0 \qquad \text{in } \Omega, \tag{46}$$

$$\mathbf{e} = \mathbb{D} : \nabla^{\text{s}} \mathbf{u} \qquad \text{in } \Omega. \tag{47}$$

We have introduced the deviatoric strains $\mathbf{e}$ in system (25)–(27) by incorporating the deviatoric constitutive Eq. (45). Furthermore, the kinematic equation for deviatoric components (47) has been added to the system to relate the displacement field $\mathbf{u}$ with the deviatoric strains $\mathbf{e}$.

Remark 2.4. Note that Eq. (45) allows us to obtain the deviatoric stresses as a function of the deviatoric strains rather than the symmetric gradient of the displacements. Therefore, we are hopefully incrementing the accuracy of the stress field $\boldsymbol{\sigma}$, which now is going to be computed as a function of both the pressure p and the deviatoric strains $\mathbf{e}$.

2.4.1. Governing equations

To complete this section, we introduce the mixed $\mathbf{u}/p/\mathbf{e}$ problem, which consists in finding a displacement field $\mathbf{u}$, a pressure p and a deviatoric strain field $\mathbf{e}$ such that

$$-\nabla \cdot \left\{\mathbb{C}^{\text{dev}} : \mathbf{e}\right\} + \nabla p = \rho \mathbf{b} \qquad \text{in } \Omega, \tag{48}$$

$$\nabla \cdot \mathbf{u} + \frac{p}{\kappa} = 0 \qquad \text{in } \Omega, \tag{49}$$

$$\mathbb{C}^{\text{dev}} : \mathbf{e} - \mathbb{C}^{\text{dev}} : \nabla^{\text{s}}\mathbf{u} = 0 \qquad \text{in } \Omega, \tag{50}$$

where the kinematic Eq. (47) has been contracted with $\mathbb{C}^{\text{dev}}$ to symmetrize the system. The governing equations must be supplied with a set of boundary conditions

$$\mathbf{u} = \mathbf{0} \qquad \text{in } \Gamma_D, \tag{51}$$

$$\boldsymbol{\sigma}\mathbf{n} \overset{(13)}{=} \left\{\mathbb{C}^{\text{dev}} : \mathbf{e}\right\}\mathbf{n} - p\mathbf{n} = \mathbf{t} \qquad \text{in } \Gamma_N, \tag{52}$$

2.4.2. Variational form of the problem

Let us consider the same spaces and tests functions we have defined previously for the mixed $\mathbf{u}/p$ problem. From the computational point of view, it is interesting to adopt Voigt's notation, which transforms the tensorial format of a generic symmetric tensor into a v-dimensional vector with $v = 3$ if $d = 2$ and $v = 6$ if $d = 3$. Let $\mathbb{E} = \left[L^2(\Omega)\right]^v$ be the proper functional space where deviatoric strain components are well-defined. We shall be interested also in the spaces $\mathbb{W} := \mathbb{V} \times \mathbb{Q} \times \mathbb{E}$, $\mathbb{W}_0 := \mathbb{V}_0 \times \mathbb{Q} \times \mathbb{E}$. The variational statement of the problem is derived by testing system (48)–(50) against arbitrary test functions $\mathbf{V} := [\mathbf{v}, q, \mathbf{f}]^T$, $\mathbf{v} \in \mathbb{V}_0^d$, $q \in \mathbb{Q}$ and $\mathbf{f} \in \mathbb{E}$. The weak form of the problem reads: find $\mathbf{U} := [\mathbf{u}, p, \mathbf{e}]^T \in \mathbb{W}_0$ such that initial conditions are satisfied and

$$\mathcal{A}(\mathbf{U}, \mathbf{V}) = \mathcal{F}(\mathbf{V}) \quad \forall \mathbf{V} \in \mathbb{W}_0, \tag{53}$$

where $\mathcal{A}(\mathbf{U}, \mathbf{V})$ is a bilinear form defined on $\mathbb{W}_0 \times \mathbb{W}_0$ as

$$\mathcal{A}(\mathbf{U}, \mathbf{V}) := \left(\nabla^s \mathbf{v}, \mathbb{C}^{\text{dev}} : \mathbf{e}\right) - (\nabla \cdot \mathbf{v}, p) + (q, \nabla \cdot \mathbf{u}) + \left(q, \frac{1}{\kappa} p\right) - \left(\mathbb{C}^{\text{dev}} : \mathbf{f}, \nabla^s \mathbf{u}\right) + \left(\mathbf{f}, \mathbb{C}^{\text{dev}} : \mathbf{e}\right). \tag{54}$$

$\mathcal{F}(\mathbf{V})$ is a linear form defined on $\mathbb{W}_0$ as

$$\mathcal{F}(\mathbf{V}) := \langle \mathbf{v}, \rho\mathbf{b} \rangle + \langle \mathbf{v}, \mathbf{t} \rangle_{\Gamma_N}. \tag{55}$$

As usual, integration by parts has been used in order to decrease the continuity requirements of the unknowns and the traction vector $\mathbf{t}$ has been identified.

2.4.3. Galerkin Spatial discretization

We can now construct a conforming finite element space $\mathbb{E}_h \subset \mathbb{E}$ and redefine $\mathbb{W}_h = \mathbb{V}_h \times \mathbb{Q}_h \times \mathbb{E}_h$ as well as the corresponding subspace $\mathbb{W}_{h,0} = \mathbb{V}_{h,0} \times \mathbb{Q}_h \times \mathbb{E}_h$ in the usual manner.

The Galerkin discrete version of problem (53) is: find $\mathbf{U}_h \in \mathbb{W}_{h,0}$ such that

$$\mathcal{A}(\mathbf{U}_h, \mathbf{V}_h) = \mathcal{F}(\mathbf{V}_h) \quad \forall \mathbf{V}_h \in \mathbb{W}_{h,0}. \tag{56}$$

This problem also requires and inf–sup condition to be satisfied between the interpolation spaces. Otherwise, instabilities may appear. In order to overcome such instabilities, we use again the stabilization technique described in next section.

Remark 2.5. In principle, we have posed no restrictions on the choice of the finite element spaces. However, let us analyze the numerical stability of problem (56). If we take $\mathbf{V}_h = \mathbf{U}_h$, it is found that

$$\mathcal{A}(\mathbf{U}_h, \mathbf{U}_h) = \left(p_h, \frac{1}{\kappa} p_h\right) + \left(\mathbf{e}_h, \mathbb{C}^{\text{dev}} : \mathbf{e}_h\right) \geq c\|\mathbf{e}_h\|^2 + \frac{1}{\kappa}\|p_h\|^2. \tag{57}$$

It is seen from Eq. (57) that $\mathcal{A}(\cdot, \cdot)$ is not coercive in $\mathbb{W}_h$, the displacement being out of control. Furthermore, in the nearly and fully incompressible cases, when $\kappa \to \infty$, also the pressure is out of control. Hence, the inf–sup condition is not satisfied independently of the incompressibility of the material.

2.4.4. Stabilized $\mathbf{u}/p/\mathbf{e}$ finite element formulation

The elements of the subscale space are now denoted by $\tilde{\mathbf{U}} \equiv \left[\tilde{\mathbf{u}}, \tilde{p}, \tilde{\mathbf{e}}\right]^T$. Taking into account that $\mathcal{A}(\cdot, \cdot)$ is a bilinear form, the continuous problem (53) is equivalent to find $\mathbf{U} \in \mathbb{W}_{h,0}$ and $\tilde{\mathbf{U}} \in \tilde{\mathbb{W}}_0$ such that

$$\mathcal{A}(\mathbf{U}_h, \mathbf{V}_h) + \mathcal{A}\left(\tilde{\mathbf{U}}, \mathbf{V}_h\right) = \mathcal{F}(\mathbf{V}_h) \qquad \forall \mathbf{V}_h \in \mathbb{W}_{h,0}, \tag{58}$$

$$\mathcal{A}\left(\mathbf{U}_h, \tilde{\mathbf{V}}\right) + \mathcal{A}\left(\tilde{\mathbf{U}}, \tilde{\mathbf{V}}\right) = \mathcal{F}\left(\tilde{\mathbf{V}}\right) \qquad \forall \tilde{\mathbf{V}} \in \tilde{\mathbb{W}}_0. \tag{59}$$

The sub-grid scale is expressed in terms of the residual of the projected (Galerkin) counterpart of Eqs. (48)–(50) to obtain

$$\tilde{\mathbf{u}} \approx \tau_{\mathbf{u}} \tilde{\Pi} \left(\nabla \cdot \left\{\mathbb{C}^{\text{dev}} : \mathbf{e}\right\} - \nabla p_h - \rho \mathbf{b}\right), \tag{60}$$

$$\tilde{p} \approx \tau_p \tilde{\Pi} \left(-\nabla \cdot \mathbf{u}_h - \frac{1}{\kappa} p_h\right), \tag{61}$$

$$\tilde{\mathbf{e}} \approx \tau_{\mathbf{e}} \tilde{\Pi} \left(\mathbb{D} : \nabla^{\text{s}} \mathbf{u}_h - \mathbf{e}_h\right), \tag{62}$$

where $\tau_{\mathbf{e}}$ is a coefficient coming from a Fourier analysis of the problem for the subscales. In this work, we use the stabilization parameters proposed in [18] for linear elastic cases

$$\tau_{\mathbf{e}} = c_3, \tag{63}$$

where c_3 is an algorithmic parameter which must be determined.

Introducing the approximate fields (60)–(62) into the finite element scale problem (58), the VMS stabilized formulation of the problem is obtained as

$$\begin{aligned} \mathcal{A}\left(\mathbf{U}_h, \mathbf{V}_h\right) &+ \sum_K \tau_{\mathbf{u}} \left\langle \nabla \cdot \left\{\mathbb{C}^{\text{dev}} : \mathbf{f}\right\} - \nabla q_h, \tilde{\Pi} \left(\nabla \cdot \mathbf{s}_h - \nabla p_h - \rho \mathbf{b}\right) \right\rangle_K \\ &+ \sum_K \tau_p \left\langle -\nabla \cdot \boldsymbol{v} + \frac{1}{\kappa} q_h, \tilde{\Pi} \left(-\nabla \cdot \mathbf{u}_h - \frac{1}{\kappa} p_h\right) \right\rangle_K \\ &+ \sum_K \tau_{\mathbf{e}} \left\langle \mathbb{C}^{\text{dev}} : \nabla^s \mathbf{v} + \mathbb{C} : \mathbf{f}, \tilde{\Pi} \left(\mathbb{D} : \nabla^{\text{s}} \mathbf{u}_h - \mathbf{e}_h\right) \right\rangle_K = \mathcal{F}\left(\mathbf{V}_h\right) \quad \forall \mathbf{V}_h \in \mathbb{W}_{h,0}. \end{aligned} \tag{64}$$

For this formulation, both the ASGS and the OSS methods are also considered.

Remark 2.6. Let us recall that the OSS stabilization allows us to include just the minimum number of terms to stabilize the solution while keeping it consistent in a weak sense. Therefore, we can reduce the stabilization terms to $\sum_K \tau_{\mathbf{u}} \left\langle \nabla q_h, \tilde{\Pi} \left(\nabla p_h\right) \right\rangle$ to stabilize the q/p component and to $\sum_K \tau_{\mathbf{e}} \left\langle \mathbb{C}^{\text{dev}} : \nabla^s \mathbf{v}, \tilde{\Pi} \left(\mathbb{D} : \nabla^{\text{s}} \mathbf{u}_h\right) \right\rangle$ to introduce stabilization terms in the $\mathbf{v}/\mathbf{u}$ part.

3. Topological derivative-based topology optimization for nearly and fully incompressible materials

3.1. Setting of the problem

In the following, the topology optimization problem is stated under the assumptions of linear elasticity and small strains. To do so, let us consider the linear elasticity system for either the $\mathbf{u}/p$ formulation (25)–(27) or the $\mathbf{u}/p/\mathbf{e}$ formulation (44)–(47). Generally speaking, the aim is to obtain an optimal topology such that it minimizes a desired functional and satisfies particular constraints.

The description of the topology is determined by the characteristic function χ, defined as

$$\chi\left(\mathbf{x}\right) = \begin{cases} 1 & \mathbf{x} \in \Omega_{\text{s}} \\ 0 & \mathbf{x} \in \Omega_{\text{w}}, \end{cases} \tag{65}$$

where the domain Ω has been split into two parts, $\overline{\Omega} = \overline{\Omega_{\text{s}} \cup \Omega_{\text{w}}}$, $\Omega_{\text{s}} \cap \Omega_{\text{w}} = \emptyset$. The sub-domains Ω_{s} and Ω_{w} are made of different materials. The characteristic function is in charge of determining in the whole domain Ω what part corresponds to either material. Such kind of problems are typically termed bi-material topology optimization problems. The material corresponding to the domain Ω_{w} exhibits a very small stiffness approximating the absence of material. The material parameters of the strong domain Ω_{s} are denoted by E_{s} and ν_{s} and the parameters of the weak domain Ω_{w} are considered as $E_{\text{w}} = \gamma E_{\text{s}}$ and ν_{w}, where γ stands for the jump of stiffness. Note that $\gamma > 0$ is a parameter, small enough for modeling void regions and large enough to entail invertibility properties to the stiffness matrix. The characteristic function allows us to rewrite the deviatoric constitutive tensor defined in the whole domain as

$$\mathbb{C}^{\text{dev}}\left(\chi\right) = \chi \mathbb{C}_{\text{s}}^{\text{dev}} + (1 - \chi) \mathbb{C}_{\text{w}}^{\text{dev}}, \tag{66}$$

where $\mathbb{C}_{\mathrm{s}}^{\mathrm{dev}}$ and $\mathbb{C}_{\mathrm{w}}^{\mathrm{dev}}$ are the fourth order deviatoric constitutive tensors of the stiff and the soft materials, respectively.

To obtain structures with minimum flexibility, a functional $\mathcal{J}(\chi)$ is minimized. In topological optimization problems this functional is usually referred to as the *total potential energy functional* and is defined as

$$\mathcal{J}(\chi) = \frac{1}{2}\int_{\Omega} \boldsymbol{\sigma}(\chi, \mathbf{x}) : \boldsymbol{\varepsilon}(\chi, \mathbf{x}) \; d\Omega - \int_{\Omega} \rho \mathbf{b} \cdot \mathbf{u}(\chi, \mathbf{x}) - \int_{\Gamma_N} \mathbf{t} \cdot \mathbf{u}(\chi, \mathbf{x}). \tag{67}$$

The whole Topology Optimization problem is then formulated as the minimization of this functional subjected to the maximum material allowed, as follows

$$\begin{aligned} &\min_{\chi \in \mathbb{X}_L} \mathcal{J}(\chi) = \frac{1}{2}\int_{\Omega} \boldsymbol{\sigma}(\chi, \mathbf{x}) : \boldsymbol{\varepsilon}(\chi, \mathbf{x}) \; d\Omega - \int_{\Omega} \rho \mathbf{b} \cdot \mathbf{u}(\chi, \mathbf{x}) - \int_{\Gamma_N} \mathbf{t} \cdot \mathbf{u}(\chi, \mathbf{x}) \\ &\text{such that} : \mathcal{A}(\mathbf{U}, \mathbf{V}) = \mathcal{F}(\mathbf{V}) \quad \forall \mathbf{V} \in \mathbb{W}_0, \\ &\mathbb{X}_L = \left\{ \chi \in L^{\infty}(\Omega, \{0, 1\}), \int_{\Omega} \chi(\mathbf{x}) \; d\Omega = L|\Omega| \right\}, \end{aligned} \tag{68}$$

where $\mathbb{X}_L$ is the space of characteristic functions, restricted to a volume constraint denoted as a fraction $0 < L < 1$ of the domain Ω, and $\mathcal{A}(\cdot, \cdot)$ and $\mathcal{F}(\cdot)$ are the bilinear and linear forms which have been obtained in Section 2 depending upon the formulation, defined as (34)–(35) for the $\mathbf{u}/p$ formulation and as (54)–(55) for the $\mathbf{u}/p/\mathbf{e}$ formulation.

3.2. Material interpolation

In the traditional bi-material topological derivative topology optimization approach, the Poisson ratio remains constant, $\nu = \nu_{\mathrm{s}} = \nu_{\mathrm{w}}$, while only the Young modulus is modified depending on the value of the characteristic function χ. For compressible materials, this approach ensures that the soft material is not notably contributing to the stiffness of the structure. However, when dealing with incompressible materials, this leads to spurious solutions, because bubbles of weak material are still infinitely stiff with respect to volumetric deformations. To avoid this, we consider the soft material as compressible, which means $\nu_{\mathrm{w}} < 0.5$. In this work, we consider that both Young's modulus and Poisson's ratio are modified depending on the value of the characteristic function.

Remark 3.1. Over the last years, a physical interpretation has been given to elements cut by the discontinuity in χ in several works [36]. They are directly related with composite materials composed with strong and weak material volume fraction. Furthermore, some physical restrictions such as the Hashin–Shtrikman bounds [37] must be fulfilled.

3.3. Topology optimization using the topological derivative concept

Several approaches exist to solve the topology optimization problem (68). In this work we use the topological derivative concept [9] together with a level-set approach in order to advance to the optimal topology.

The topological derivative is a measurement of the sensitivity of a given functional with respect to the apparition of an infinitesimal inclusion in a given point of the domain of interest. In the problem studied, the objective is to obtain the sensitivity of the functional $\mathcal{J}(\chi)$. The topological derivative $\mathcal{D}_T \mathcal{J}(\chi, \mathbf{x})$ of this functional at a point $\mathbf{x}$ can be formally computed as

$$\mathcal{D}_T \mathcal{J}(\chi, \mathbf{x}) = \boldsymbol{\varepsilon}(\chi, \mathbf{x}) : \mathbb{P} : \boldsymbol{\sigma}(\chi, \mathbf{x}) + (1 - \gamma)\rho \mathbf{b} \cdot \mathbf{u}(\chi, \mathbf{x}), \tag{69}$$

using the *topological-shape sensitivity analysis* proposed in [32]. In the given equation, $\mathbb{P}$ stands for the fourth order *Pólya–Szegő* polarization tensor. In this work, the classical Polarization tensor expression, in which the same Poisson coefficient is assumed for both materials, is not suitable (see Section 3.2). According to [38], the Polarization tensor is defined as

$$\mathbb{P} = \frac{1}{2}\Delta\mathbb{C} : \left\{ \mathbb{C}_{\mathrm{e}}^{-1} + \mathbb{C}_{\mathrm{i}}^{-1} : \mathbb{T} \right\}, \tag{70}$$

where $\mathbb{C}_{\mathrm{i}}$ accounts for the constitutive tensor of the inclusion and $\mathbb{C}_{\mathrm{e}}$ for the matrix material. Furthermore $\Delta\mathbb{C} := \mathbb{C}_{\mathrm{i}} - \mathbb{C}_{\mathrm{e}}$ and $\mathbb{T}$ is a 4th-order isotropic tensor called the Eshelby tensor, originating from Eshelby's Theorem [39,40].

The Eshelby tensor allows us to relate the stresses in the inclusion with the ones from the matrix material. To build the Eshelby tensor $\mathbb{T}$, it is necessary to solve an equilibrium equation in Linear Elasticity. Two different bodies are considered (inclusion and matrix) with different Young's modulus and Poisson's ratios. It must be imposed that very far from the inclusion, the stresses cancel out for the matrix. Then, we impose the Eshelby theorem for the inclusion material, which asserts that the strain field inside the inclusion is constant if the loading at infinity is constant (zero in this case). Once the boundary conditions are imposed in both solids, the transmission conditions across the interface of the inclusion and the matrix must be satisfied. Regarding the stresses, the exterior problem is defined such that the jump of the traction across the interface must be equal to the normal component of the given stress tensor. Regarding the transmission conditions on displacements, we must ensure that the jump of the strains across the boundary must be zero for the inclusion. This problem is solved via symbolic calculus. Once the Eshelby tensor is obtained, the computation of the Polarization tensor is straightforward.

Considering a plane strain scenario, the Polarization tensor is computed as

$$\mathbb{P} = -\frac{1}{2}(1+\beta)\left\{\frac{\tau_1-\gamma}{\beta\gamma+\tau_1}\mathbb{I} - \frac{1}{4}\left(\frac{\alpha(\gamma-\tau_1\tau_2)}{\alpha\gamma+\tau_1\tau_2} + \frac{2(\tau_1-\gamma)}{\beta\gamma+\tau_1}\right)\mathbf{I}\otimes\mathbf{I}\right\}, \tag{71}$$

where

$$\alpha = \frac{1}{1-2\nu_e}, \quad \beta = 3-4\nu_e, \quad \tau_1 = \frac{1+\nu_i}{1+\nu_e} \quad \text{and} \quad \tau_2 = \frac{1-2\nu_i}{1-2\nu_e}. \tag{72}$$

Considering a plane stress scenario on the other hand,

$$\mathbb{P} = -\frac{1}{2}(1+\beta)\left\{\frac{\tau_1-\gamma}{\beta\gamma+\tau_1}\mathbb{I} - \frac{1}{4}\left(\frac{\gamma(\alpha+\tau_2-1)-\alpha\tau_1\tau_2}{\tau_1(\alpha\gamma+\tau_2)} + \frac{2(\tau_1-\gamma)}{\beta\gamma+\tau_1}\right)\mathbf{I}\otimes\mathbf{I}\right\} \tag{73}$$

and

$$\alpha = \frac{1+\nu_e}{1-\nu_e}, \quad \beta = \frac{3-\nu_e}{1+\nu_e}, \quad \tau_1 = \frac{1+\nu_i}{1+\nu_e} \quad \text{and} \quad \tau_2 = \frac{1-\nu_i}{1-\nu_e}. \tag{74}$$

Independently from the strain/stress assumption, the jump of stiffness is defined as $\gamma = E_w/E_s$, while ν_e and ν_i are the Poisson ratios of the matrix and inclusion material.

Remark 3.2. If the same Poisson ratio is used for both materials $\nu_s = \nu_w$, and therefore, $\nu_i = \nu_e$, the Polarization tensors (71) and (73) reduce to

$$\mathbb{P} = -\frac{1}{2}\frac{1-\gamma}{1+\beta\gamma}\left\{(1+\beta)\mathbb{I} + \frac{1}{2}(\alpha-\beta)\frac{1-\gamma}{1+\alpha\gamma}\mathbf{I}\otimes\mathbf{I}\right\}, \tag{75}$$

which is the formulation widely used in structural topological design [41].

In this work, the isotropic 2D plane strain polarization tensor has been used as an approximation for the 3D polarization tensor. By using this approximation, infinitesimal cylindrical inclusions are considered instead of spherical ones in the derivation of the topological derivative. Although spherical inclusions would be more appropriate, experience shows that infinitesimal cylindrical inclusions behave properly in 3D examples [8].

Considering a domain with weak and strong material, we can expect the following two situations:

(1) an inclusion of the weak material in the strong material ($\mathbf{x} \in \Omega_s$),
(2) an inclusion of the strong material in the weak material ($\mathbf{x} \in \Omega_w$).

Consequently, rewriting the polarization tensor as $\mathbb{P}(\alpha, \beta, \gamma, \tau_1, \tau_2)$, both cases share the following properties

$$\mathbb{P} = \begin{cases} \mathbb{P}_s := \mathbb{P}(\alpha_s, \beta_s, \gamma, \tau_1, \tau_2) & \mathbf{x} \in \Omega_s \\ \mathbb{P}_w := \mathbb{P}\left(\alpha_w, \beta_w, \frac{1}{\gamma}, \frac{1}{\tau_1}, \frac{1}{\tau_2}\right) & \mathbf{x} \in \Omega_w. \end{cases} \tag{76}$$

where α_s and β_s are the Polarization parameters evaluated for ν_s and α_w and β_w evaluated for ν_w.

The properties of the polarization tensor ensure that

$$\mathcal{D}_T\mathcal{J}(\chi,\mathbf{x}) = \begin{cases} \boldsymbol{\varepsilon}(\chi,\mathbf{x}) : \mathbb{P}_s : \boldsymbol{\sigma}(\chi,\mathbf{x}) + (1-\gamma)\rho\mathbf{b}\cdot\mathbf{u}(\chi,\mathbf{x}) \leq 0 & \forall \mathbf{x} \in \Omega_s \\ \boldsymbol{\varepsilon}(\chi,\mathbf{x}) : \mathbb{P}_w : \boldsymbol{\sigma}(\chi,\mathbf{x}) + (1-\gamma)\rho\mathbf{b}\cdot\mathbf{u}(\chi,\mathbf{x}) \geq 0 & \forall \mathbf{x} \in \Omega_w. \end{cases} \tag{77}$$

We can now define a signed topological derivative such that

$$\overline{\mathcal{D}_T\mathcal{J}}(\chi,\mathbf{x}) = \begin{cases} -\mathcal{D}_T\mathcal{J}(\chi,\mathbf{x}) & \mathbf{x} \in \Omega_s \\ \mathcal{D}_T\mathcal{J}(\chi,\mathbf{x}) & \mathbf{x} \in \Omega_w. \end{cases} \tag{78}$$

Let us now introduce the signed topological derivative interpretation, which will be used in the subsequent sections of this work. For a given topology, computing the topological derivative allows one to know, for each given spatial point, how the cost functional would change if the material switches. Once the optimal value for the characteristic function $\chi(\mathbf{x})$ has been reached, the following condition holds

$$\overline{\mathcal{D}_T\mathcal{J}}(\chi,\mathbf{x}) \geq \overline{\mathcal{D}_T\mathcal{J}}(\chi,\mathbf{y}), \forall \mathbf{x} \in \Omega_s, \forall \mathbf{y} \in \Omega_w. \tag{79}$$

Note that at the interface $\overline{\Omega_s} \cap \overline{\Omega_w}$, the topological derivative has a jump, but the signed topological derivative is continuous. Eq. (79) allows one to construct a level set function $\psi(\chi,\mathbf{x})$, which will implicitly characterize Ω_s and Ω_w. This level set function is defined as

$$\psi(\chi,\mathbf{x}) = \overline{\mathcal{D}_T\mathcal{J}}(\chi,\mathbf{x}) + \lambda, \tag{80}$$

where $\lambda \in \mathbb{R}$ is a scalar, responsible for ensuring that the volume restriction in Eq. (68) is fulfilled. The level-set function also allows us to characterize the description of the topology

$$\psi(\chi,\mathbf{x}) \begin{cases} > 0 & \mathbf{x} \in \Omega_s \\ < 0 & \mathbf{x} \in \Omega_w. \end{cases} \tag{81}$$

Furthermore, the level-set function allows us to keep a sharp interface when $\psi(\chi,\mathbf{x}) = 0$. The scalar λ can be computed by enforcing

$$\int_\Omega H(\psi(\chi,\mathbf{x}))\, d\Omega = L|\Omega|, \tag{82}$$

where $H(\cdot)$ is the Heaviside step function

$$H(\psi) = \begin{cases} 1 & \text{if } \psi \geq 0 \\ 0 & \text{if } \psi < 0. \end{cases} \tag{83}$$

From Eqs. (81) and (83), it can be observed that for the solution of Eq. (68) there holds:

$$\chi = H(\psi). \tag{84}$$

Remark 3.3. When considering the finite element approximation of the problem, an inconsistency appears in the update of the level-set function in Eq. (80). According to expressions (71), (73), the topological derivative depends directly on the stresses and strains. Clearly, this kind of functions are not continuous which is, in fact, the requirement for updating the level-set function $\psi(\chi,\mathbf{x})$. As a remedy, an element-to-nodal regularization must be considered. The regularization is carried out by a projection onto the finite element space (smoothing operation) but this results in a loss of a certain degree of accuracy. Nevertheless, the level-set updating (80) is now possible. In [42] a smoothing of the interface for projecting the topological derivative onto the finite element space is proposed, which allows one to still interpret the topological derivative as an exact discrete gradient.

3.4. Topological derivative for incompressible materials

Referring to expression (71), which is valid for both plane strain and 3D scenarios, we observe that the Polarization tensor becomes ill-defined due to the fact that when $\nu_e \to 0.5$, $\alpha = \frac{1}{1-2\nu_e} \to \infty$. It can be clearly seen that the Polarization tensor cannot be used to compute the topological derivative for incompressible materials in both

cases. In order to deal with nearly and fully incompressible materials we propose to apply the deviatoric–volumetric split to the Polarization tensor as well. The volumetric and deviatoric counterparts of the Polarization tensor are

$$\mathbb{P}^{\text{vol}} = \mathbb{V} : \mathbb{P} = \frac{\alpha\,(1+\beta)}{8}\frac{\gamma - \tau_1\tau_2}{\alpha\gamma + \tau_1\tau_2}\mathbf{I}\otimes\mathbf{I}, \tag{85}$$

$$\mathbb{P}^{\text{dev}} = \mathbb{D} : \mathbb{P} = -\frac{1}{2}\frac{(1+\beta)(\tau_1 - \gamma)}{\tau_1 + \beta\gamma}\left\{\mathbb{I} - \frac{1}{3}\mathbf{I}\otimes\mathbf{I}\right\}, \tag{86}$$

$$\mathbb{P} = \mathbb{P}^{\text{vol}} + \mathbb{P}^{\text{dev}}. \tag{87}$$

Next, we can use the Polarization tensor decomposition to compute the topological derivative as

$$\begin{aligned}
\mathcal{D}_T\mathcal{J}\,(\chi,\mathbf{x}) = \;& \boldsymbol{\varepsilon}\,(\chi,\mathbf{x}) : \mathbb{P} : \boldsymbol{\sigma}\,(\chi,\mathbf{x}) + (1-\gamma)\rho\mathbf{b}\cdot\mathbf{u}\,(\chi,\mathbf{x}) \\
\overset{(87)}{=}\; & \boldsymbol{\varepsilon}\,(\chi,\mathbf{x}) : \left\{\mathbb{P}^{\text{vol}} + \mathbb{P}^{\text{dev}}\right\} : \boldsymbol{\sigma}\,(\chi,\mathbf{x}) + (1-\gamma)\rho\mathbf{b}\cdot\mathbf{u}\,(\chi,\mathbf{x}) \\
\overset{(13)}{=}\; & \boldsymbol{\varepsilon}\,(\chi,\mathbf{x}) : \left\{\mathbb{P}^{\text{vol}} + \mathbb{P}^{\text{dev}}\right\} : \{\mathbf{s}\,(\chi,\mathbf{x}) - p\,(\chi,\mathbf{x})\,\mathbf{I}\} + (1-\gamma)\rho\mathbf{b}\cdot\mathbf{u}\,(\chi,\mathbf{x}) \\
=\; & \boldsymbol{\varepsilon}\,(\chi,\mathbf{x}) : \mathbb{P}^{\text{dev}} : \mathbf{s}\,(\chi,\mathbf{x}) - \boldsymbol{\varepsilon}\,(\chi,\mathbf{x}) : \mathbb{P}^{\text{vol}} : p\,(\chi,\mathbf{x})\,\mathbf{I} + (1-\gamma)\rho\mathbf{b}\cdot\mathbf{u}\,(\chi,\mathbf{x})\,.
\end{aligned} \tag{88}$$

The last equation holds by imposing that the contraction between volumetric and deviatoric tensors is identically null. This fact allows to reduce the formulation further.

It is worth to study the first two components of the decomposed topological derivative (88) in detail. The first summand accounts for the topological derivative due to deviatoric effects. By introducing the strain field decomposition (15) we can reduce it to

$$\boldsymbol{\varepsilon}\,(\chi,\mathbf{x}) : \mathbb{P}^{\text{dev}} : \mathbf{s}\,(\chi,\mathbf{x}) = \left\{\frac{1}{3}e^{\text{vol}}\,(\chi,\mathbf{x})\,\mathbf{I} + \mathbf{e}\,(\chi,\mathbf{x})\right\} : \mathbb{P}^{\text{dev}} : \mathbf{s}\,(\chi,\mathbf{x}) = \mathbf{e}\,(\chi,\mathbf{x}) : \mathbb{P}^{\text{dev}} : \mathbf{s}\,(\chi,\mathbf{x})\,. \tag{89}$$

The second summand in Eq. (88) accounts for the topological derivative changes due to volumetric deformations. To solve the singularity which $\mathbb{P}^{\text{vol}}$ still presents when dealing with nearly and fully incompressible materials, we need to introduce the pressure field as

$$\begin{aligned}
-\boldsymbol{\varepsilon}\,(\chi,\mathbf{x}) : \mathbb{P}^{\text{vol}} : p\,(\chi,\mathbf{x})\,\mathbf{I} = \;& -e^{\text{vol}}\,(\chi,\mathbf{x})\cdot p\,(\chi,\mathbf{x})\,\mathbf{I} : \mathbb{P}^{\text{vol}} : \mathbf{I} \\
\overset{(16)}{=}\; & -\nabla\cdot\mathbf{u}\,(\chi,\mathbf{x})\cdot p\,(\chi,\mathbf{x})\,\mathbf{I} : \mathbb{P}^{\text{vol}} : \mathbf{I} \\
\overset{(23)}{=}\; & \frac{p\,(\chi,\mathbf{x})}{\kappa_{\text{e}}}\cdot p\,(\chi,\mathbf{x})\,\mathbf{I} : \mathbb{P}^{\text{vol}} : \mathbf{I} \\
=\; & \left\{\frac{1}{\kappa_{\text{e}}}\mathbf{I} : \mathbb{P}^{\text{vol}} : \mathbf{I}\right\} p^2\,(\chi,\mathbf{x}) \\
\coloneqq\; & \mathrm{P}^{\text{vol}} p^2\,(\chi,\mathbf{x})\,,
\end{aligned} \tag{90}$$

where κ_{e} is the bulk modulus of the matrix material and P^{vol} is defined as the volumetric Polarization parameter and it is expressed as

$$\mathrm{P}^{\text{vol}} = \frac{1}{\kappa_{\text{e}}}\mathbf{I} : \mathbb{P}^{\text{vol}} : \mathbf{I} = \frac{1+\beta}{E_{\text{e}}}\frac{\gamma - \tau_1\tau_2}{\alpha\gamma + \tau_1\tau_2}. \tag{91}$$

By introducing the compressibility modulus κ_{e} in the volumetric part of the polarization tensor, we have solved the singularity that $\mathbb{P}^{\text{vol}}$ is presenting.

Remark 3.4. In the incompressible limit, no volumetric changes should appear when both materials are incompressible. Therefore, the contribution to the topological derivative made by P^{vol} must be zero when $\nu = \nu_{\text{e}} = \nu_{\text{i}} = 0.5$. Indeed, we have that

$$\mathrm{P}^{\text{vol}}\big|_{\nu=0.5} = \frac{1+\beta}{E_{\text{e}}}\frac{\gamma-1}{\alpha\gamma+1} = \frac{4-4\nu}{E_{\text{e}}}\frac{\gamma-1}{\frac{1}{1-2\nu}\gamma+1} = \frac{2}{E_{\text{e}}}\frac{\gamma-1}{\frac{1}{0}\gamma+1} = 0 \tag{92}$$

Note that in this case, volumetric effects vanish and the topology optimization problem is only driven by deviatoric changes.

Finally, the formula for the split topological derivative, which is valid for nearly and fully incompressible materials and applicable in plane strain and 3D scenarios, is given as

$$\mathcal{D}_T \mathcal{J}(\chi, \mathbf{x}) = \mathbf{e}(\chi, \mathbf{x}) : \mathbb{P}^{\text{dev}} : \mathbf{s}(\chi, \mathbf{x}) + \mathrm{P}^{\text{vol}} p^2(\chi, \mathbf{x}) + (1-\gamma)\rho \mathbf{b} \cdot \mathbf{u}(\chi, \mathbf{x}). \tag{93}$$

Remark 3.5. It is worth pointing out the main differences between the two mixed formulations with regard to the split topological derivative, shown in Eq. (93). When considering the $\mathbf{u}/p$ formulation, both deviatoric stresses and strains are computed from the symmetric gradient of the displacements $\nabla^{\text{s}}\mathbf{u}$, whereas when using the $\mathbf{u}/p/\mathbf{e}$ formulation, deviatoric stresses are now computed from deviatoric strains $\mathbf{e}$ which are an unknown of the problem. Therefore, the computation of the topological derivative is expected to be more accurate.

3.5. Treatment of the interface elements

Let us discuss an issue related to the finite element approximation of the problem. Interface elements belong partially to the strong and partially to the weak domain. These elements are therefore characterized by the material properties of both domains and special attention needs to be payed to the behavior of the topological derivative in those elements. In order to obtain the correct combination of material properties, a homogenization technique is used.

Let us construct a conforming finite element mesh $\mathcal{M}$, composed of N elements and let us also split the domain into three different sub-groups:

(1) elements which fully lie in the domain associated with the strong material $\mathcal{T}_{\text{s}}$,
(2) elements which fully lie in the domain associated with the weak material $\mathcal{T}_{\text{w}}$, and
(3) elements intersecting the interface, thus sharing both materials $\mathcal{T}^{\Gamma}$.

The description of the interface is based on the treatment of the characteristic function $\chi(\mathbf{x})$, which, in turn, is based on the treatment of the level-set function $\psi(\chi, \mathbf{x})$. For the description, two different approaches are commonly used in topology optimization when using the topological derivative: the *In-or-Out* approach and the P1-projection approach [7,43]. In our work a third option, the continuous regularized characteristic function approach, is used.

Let us denote by K^{Γ} the volume of an interface element in $\mathcal{T}^{\Gamma}$. K_{s}^{Γ} and K_{w}^{Γ} are the subdivisions with strong and weak material obtained for that specific element when it is cut by the level-set function. Then we can define the volume fraction of stiff and soft materials as

$$\mathcal{V}_{\text{s}} = \frac{K_{\text{s}}^{\Gamma}}{K^{\Gamma}} \in (0,1) \quad \text{and} \quad \mathcal{V}_{\text{w}} = \frac{K_{\text{w}}^{\Gamma}}{K^{\Gamma}} = 1 - \mathcal{V}_{\text{s}} \in (0,1). \tag{94}$$

Furthermore we can redefine the regularized characteristic function as the volume fraction of the strong material, i.e.

$$\tilde{\chi}(\mathbf{x}) = \frac{K_{\text{s}}^{\Gamma}}{K^{\Gamma}}, \quad \mathbf{x} \in K^{\Gamma}. \tag{95}$$

Note that when the element fully lies in the domain, associated with the strong material $K_{\text{s}}^{\Gamma}/K^{\Gamma} = 1$. In the opposite case the ratio becomes $K_{\text{s}}^{\Gamma}/K^{\Gamma} = 0$. Whenever an element is cut by the level-set function, we obtain a value between 0 and 1. This definition matches the characteristic function we have defined in Eq. (65). We can now compute the constitutive tensor of the element according to Eq. (66).

Remark 3.6. In comparison with other approaches, the regularized characteristic function approach evolves continuously when moving the level-set function. Consequently the deviatoric constitutive tensor varies between $\mathbb{C}_{\text{w}}^{\text{dev}}$ and $\mathbb{C}_{\text{s}}^{\text{dev}}$ at the interface between materials.

Remark 3.7. With regard to the material interpolation in the elements intersecting the interface, in this work we favor to modify the Young modulus depending upon the regularized characteristic function and to use as Poisson's coefficient the one of the strong material.

Next, we can compute stresses and strains according this new, regularized characteristic function, thus allowing us to obtain continuous values of the properties for the interface elements. The deviatoric Polarization tensor and the volumetric Polarizations parameter for elements K^Γ are defined as

$$\mathbb{P}^{\text{dev}} = \frac{K_{\text{s}}^\Gamma}{K^\Gamma}\mathbb{P}_{\text{s}}^{\text{dev}} + \left(1 - \frac{K_{\text{s}}^\Gamma}{K^\Gamma}\right)\mathbb{P}_{\text{w}}^{\text{dev}}, \quad \text{P}^{\text{vol}} = \frac{K_{\text{s}}^\Gamma}{K^\Gamma}\text{P}_{\text{s}}^{\text{vol}} + \left(1 - \frac{K_{\text{s}}^\Gamma}{K^\Gamma}\right)\text{P}_{\text{w}}^{\text{vol}}. \tag{96}$$

Finally, the split topological derivative is also computed according to Eq. (93)

4. The topology optimization algorithm

The last required ingredient is an algorithm to arrive to the solution of problem (68). In this work, we apply the iterative topology optimization algorithm as it is defined in [8]. The sequence of the individual steps is shown in the flowchart displayed in Fig. 1 and explained in more detail afterwards.

Initially, a level set function $\psi\,(\mathbf{x})$ is defined with unit initial value, which means that we consider the structure to be composed of strong material everywhere. Obviously, this first approach does not fulfill the volume constraint.

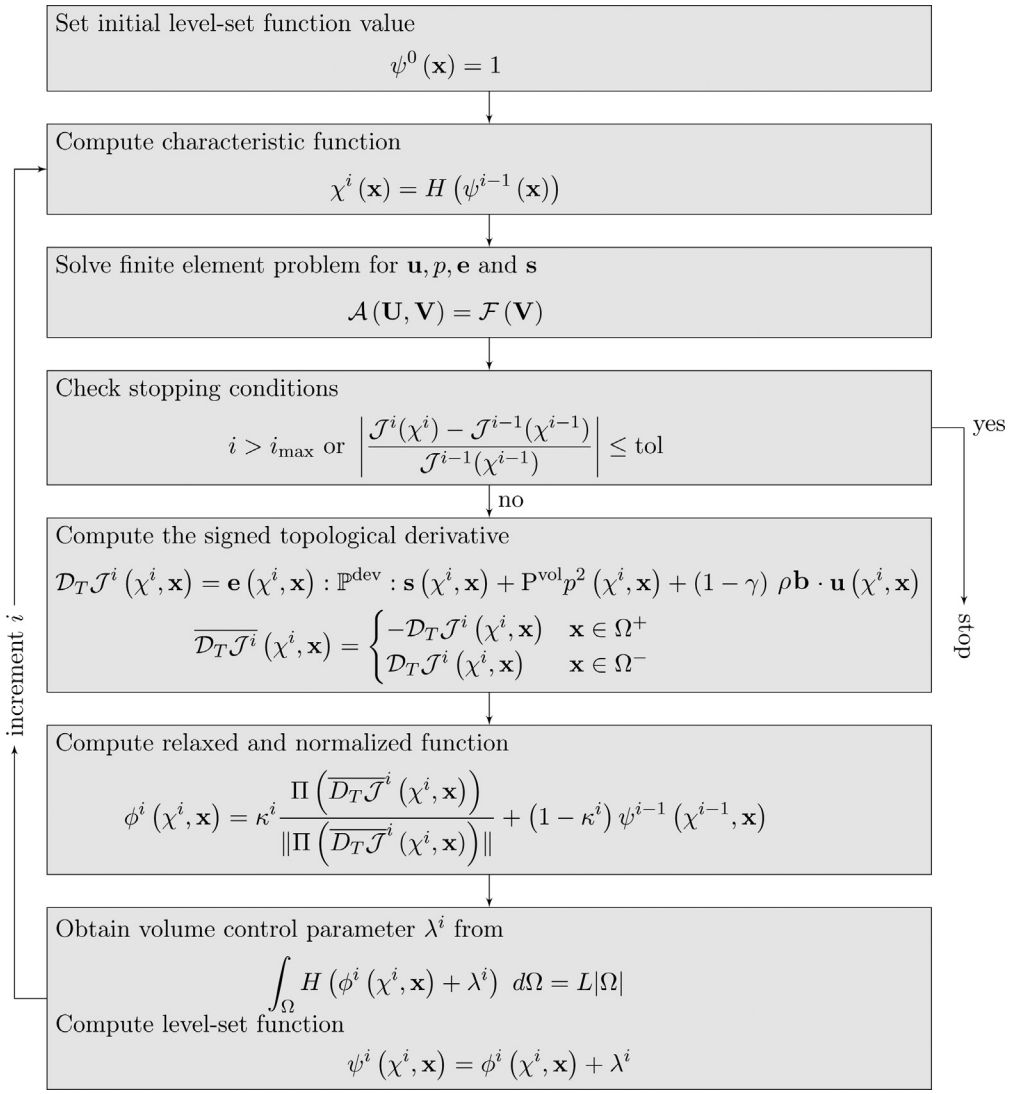

Fig. 1. Topology Optimization Algorithm Flowchart.

We thus take

$$\psi^0(\mathbf{x}) = 1 \quad \text{in } \Omega.$$

Let $\psi^{i-1}(\mathbf{x})$ a known level set, where the superscript indicates the iteration counter. From this level set value, a characteristic function can be built:

$$\chi^i(\mathbf{x}) = H\left(\psi^{i-1}(\mathbf{x})\right) \quad \text{in } \Omega, \tag{97}$$

which allows one to solve the solid mechanics problem and compute the signed topological derivative $\overline{D_T \mathcal{J}^i}\left(\chi^i, \mathbf{x}\right)$. This is independent from the use of the $\mathbf{u}/p$ or the $\mathbf{u}/p/\mathbf{e}$ formulation. For convergence aspects, the algorithm also requires an intermediate function $\phi^i\left(\chi^i, \mathbf{x}\right)$. This function is initially defined as the projection onto the finite element space of the normalized topological derivative in order to bound the level-set function with a relaxation scheme introduced as the iterative process advances, i.e.

$$\phi^i\left(\chi^i, \mathbf{x}\right) = \kappa^i \frac{\Pi\left(\overline{D_T \mathcal{J}}^i\left(\chi^i, \mathbf{x}\right)\right)}{\| \Pi\left(\overline{D_T \mathcal{J}}^i\left(\chi^i, \mathbf{x}\right)\right) \|} + \left(1 - \kappa^i\right) \psi^{i-1}\left(\chi^{i-1}, \mathbf{x}\right). \tag{98}$$

The relaxation parameter κ^i is computed according to [8], and Π indicates a projection onto the finite element space. In the numerical examples, Π is computed by using a lumped mass matrix approach for computational efficiency. This approach plays the role of standard filtering in topology optimization. Finally, the level set function at the current iteration is defined as

$$\psi^i\left(\chi^i, \mathbf{x}\right) = \phi^i\left(\chi^i, \mathbf{x}\right) + \lambda^i, \tag{99}$$

where λ^i is computed by using the secant method to solve the volume constraint equation

$$\int_\Omega H\left(\psi^i\left(\chi^i, \mathbf{x}\right)\right) \, d\Omega = L|\Omega|. \tag{100}$$

As a stopping criteria we consider the evolution of the objective functional. The algorithm concludes if the functional has not decreased by a large enough amount. Also, a maximum number of iterations to be performed is set.

To determine κ^i, a spatial oscillation indicator is computed

$$\xi^i\left(\chi^i, \mathbf{x}\right) = \text{sign}\left\{ \frac{\frac{\Pi\left(\overline{D_T \mathcal{J}}^i\left(\chi^i, \mathbf{x}\right)\right)}{\| \Pi\left(\overline{D_T \mathcal{J}}^i\left(\chi^i, \mathbf{x}\right)\right) \|} - \psi^{i-1}\left(\chi^{i-1}, \mathbf{x}\right)}{\psi^{i-1}\left(\chi^{i-1}, \mathbf{x}\right) - \psi^{i-2}\left(\chi^{i-2}, \mathbf{x}\right)} \right\}. \tag{101}$$

Note that $\xi^i\left(\chi^i, \mathbf{x}\right) = 1$, if the iterative algorithm for computing the topological derivative is advancing monotonically in the preceding iterations and $\xi^i\left(\chi^i, \mathbf{x}\right) = -1$ otherwise. This indicator allows one to detect if there are oscillations in the iterative process. If there are oscillations, the value for κ^i needs to be decreased, otherwise it can be increased up to a maximum of 1. An intermediate function $\mu^i\left(\chi^i, \mathbf{x}\right)$ is introduced as

$$\mu^i\left(\chi^i, \mathbf{x}\right) = \begin{cases} k_1 \kappa^{i-1} & \text{if } \xi^i\left(\chi^i, \mathbf{x}\right) = 1 \\ k_2 \kappa^{i-1} & \text{if } \xi^i\left(\chi^i, \mathbf{x}\right) = -1 \end{cases} \tag{102}$$

Since $\xi^i\left(\chi^i, \mathbf{x}\right)$ is a spatial function, the information on the oscillations needs to be averaged so that a scalar value for κ^i can be obtained, which is done as follows

$$\kappa^i = \min\left\{ \left(\frac{\int_\Omega \left(\mu^i\left(\chi^i, \mathbf{x}\right)\right)^{k_3} \, d\Omega}{\int_\Omega \psi^i\left(\chi^i, \mathbf{x}\right) \, d\Omega} \right)^{-k_3}, 1 \right\}, \tag{103}$$

where $k_1 \geq 1$, $k_2 \leq 1$ and $k_3 \leq 1$ are algorithmic parameters. In the numerical examples $k_1 = 1.1$, $k_2 = 0.5$ and $k_3 = 0.1$ are used.

Remark 4.1. The volume restriction is exactly fulfilled at every iteration of the algorithm unlike in alternative options. In our experience, this provides a higher global algorithmic robustness.

Remark 4.2. The relaxation parameter κ^i is evaluated node-to-node to observe the evolution of the topology optimization algorithm. The spatial oscillation indicator allows us to identify those nodes which are changing their material phase between iterations. Then, we are able to slow down the relaxation scheme by introducing the weighted average Eq. (103).

Remark 4.3. The line search algorithm we propose is not ensuring a monotonic decrease of the cost function: the topological derivative marks a direction in which the cost is going to decrease, but if we advance too much in that direction (and then we are far away from the point where the topological derivative is computed) there is no guarantee that the cost is going to decrease in that iteration. This could be achieved by not allowing the algorithm to progress until the κ^i parameter is sufficiently small and the cost function decreases. However, in our experience the algorithm that we propose, even if not monotonic, performs well and reaches a locally optimum solution [44].

5. Numerical examples

In this section, four numerical examples are presented to assess the performance of the proposed formulation. The first case we consider is a simple test with different Poisson's ratio for the strong material ν_s in order to analyze the evolution of the different formulations while increasing the incompressibility of the strong material. Next, so as to analyze the effect of considering either an incompressible weak material $\nu_w = 0.5$ or a compressible weak one $\nu_w = 0.4$, we study the optimized structure of a bearing device which is obtained for both scenarios. Thereafter, a L-shaped beam is explored in order to highlight the main differences between the $\mathbf{u}/p$ and the $\mathbf{u}/p/\mathbf{e}$ formulations. To end up, a 3D cantilever beam is studied to show the behavior of our topology optimization algorithm in a 3D case.

With regard to the stabilization methods both of them are applied interchangeably. No specification is given due to the fact that no significant differences appear in the final results, as it is expected. For all subsequent numerical examples, the algorithmic parameters are set to $c_1 = 4$, $c_2 = 2$ and $c_3 = 0.1$. Unless otherwise specified, the weak material is considered to be compressible, with $\nu_w = 0.4$. The jump of stiffness γ is fixed to 10^{-3}. In all the examples presented, continuous linear interpolation is used for all the unknowns (P_1 elements), both in the $\mathbf{u}/p$ and in the $\mathbf{u}/p/\mathbf{e}$ formulations. In these examples, the functional to be minimized is the compliance, which in the absence of body forces has twice the topological derivative of the total potential energy and thus yields the same optimal solution (see Eq. (93)). As a stopping criterion, we impose a relative tolerance for the objective functional $\text{tol} = 10^{-3}$, unless otherwise specified. In all presented figures, only the positive part of the level set is plotted, therefore only the strong material part is shown. The rest is fulfilled of weak material elements which is interpreted as the void region.

It is worth to comment about the computational efficiency of the $\mathbf{u}/p$ and the $\mathbf{u}/p/\mathbf{e}$ formulations. For the different cases we have run, more or less between the double and triple of time is needed to solve the algebraic system for the $\mathbf{u}/p/\mathbf{e}$ problem with respect to the $\mathbf{u}/p$ one, depending upon spacial dimensions and number of nodes. Despite this, it has been shown previously in the literature that in many cases it pays off to use the $\mathbf{u}/p/\mathbf{e}$ formulation, although this is not the objective of the paper and we do not perform this kind of analysis. In [18,19,25,35] the main advantages and drawbacks of several mixed formulations are presented and some situations in which the extra accuracy in the computation of the stresses is crucial are shown. For the 2D numerical examples we used direct solvers [45,46]. In the 3D final case, the number of degrees of freedom is quite big to use a direct solver. Then we moved to iterative solvers from the PETSc package with preconditioners in the u/p/e case [47].

5.1. Single-point load beam

As a first example, we study the topology optimization process for a clamped–clamped beam with a single-point load (Fig. 2). The problem consists of a rectangular panel, clamped in both the left and the right sides and subjected to a single-point vertical load $F = 3$ N at the middle of the free bottom edge. Stress free boundary conditions are applied on the remaining boundaries. We consider a linear elastic material with a Young Modulus $E_s = 30$ Pa.

Exploiting the symmetry of the structure only the left half of the original domain has been discretized using about 51,200 linear triangular elements. The required final volume is set to be 40% of the initial one. Let us mention that all figures only show the left half of the clamped beam.

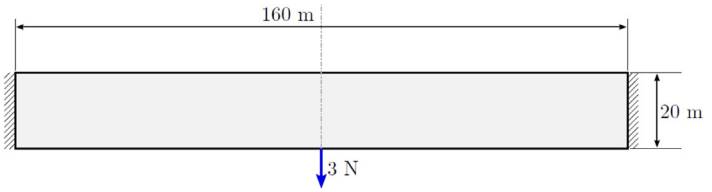

Fig. 2. Single-point load beam. Geometry.

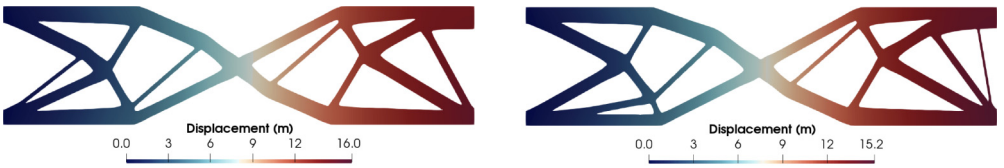

(A) $\nu_s = 0.4$ (B) $\nu_s = 0.5$

Fig. 3. Single-point load beam. Final optimized structure in plane stress scenario.

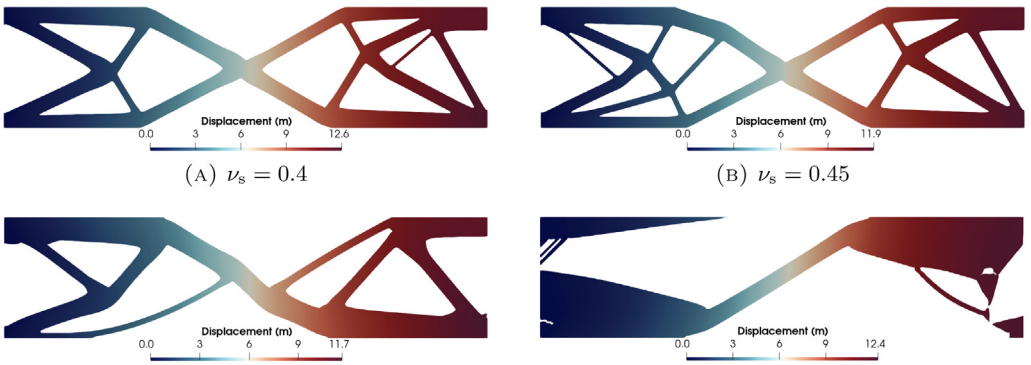

(A) $\nu_s = 0.4$ (B) $\nu_s = 0.45$

(C) $\nu_s = 0.49$ (D) $\nu_s = 0.4999$

Fig. 4. Single-point load beam. Final optimized structure in plane strain scenario while increasing the incompressibility of the stiff material.

First of all, let us consider the displacement-based formulation in a plane stress scenario. As explained in Section 3, considering plane stress, the topology optimization problem presents no singularities when the incompressible limit is reached. Therefore, even when using the *standard irreducible* formulation, no numerical issues appear in this case. Fig. 3 shows the final optimized structure for both a compressible strong material $\nu_s = 0.4$ and a fully incompressible one, $\nu_s = 0.5$. As it can be observed, a well-defined solution is reached regardless of the incompressibility of the stiff material.

Let us now move to solutions obtained in a plane strain scenario. Fig. 4 displays the evolution of the final optimized structure when increasing the incompressibility of the strong material. As expected, the obtained result is feasible when dealing with compressible materials as it can be observed in Figs. 4(a)–4(b). However, when the incompressibility of the stiff material is increased to a level high enough to consider the material almost incompressible, the algorithm fails to produce a physically plausible structure (Figs. 4(c)–4(d)). This phenomenon is caused by the singularities that appear in the incompressibility limit for both the displacement-based formulation (7) and the Polarization tensor expression (71).

Let us now apply stabilized mixed formulations with the already-defined split topological derivative expression (93). Figs. 5 and 6 show both displacement and pressure fields of the final optimized structure, obtained with the $\mathbf{u}/p$ and $\mathbf{u}/p/\mathbf{e}$ formulations, respectively, when considering compressible materials. Both figures show almost the same solution, compared to the one obtained with a displacement-based formulation, shown in Figs. 4(a)–4(b).

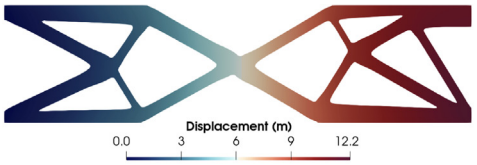

(A) $\nu_s = 0.4$. Displacement field (m)

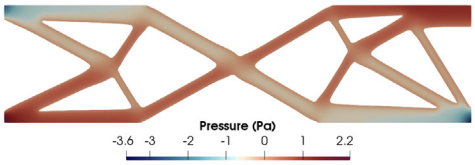

(B) $\nu_s = 0.4$. Pressure field (Pa)

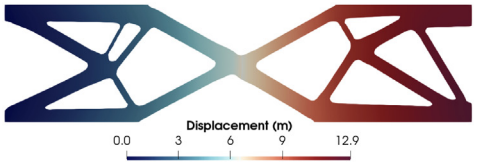

(C) $\nu_s = 0.45$. Displacement field (m)

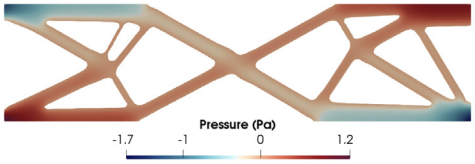

(D) $\nu_s = 0.45$. Pressure field (Pa)

Fig. 5. Single-point load beam. Final optimized structure in plane strain scenario for compressible materials with $\mathbf{u}/p$ formulation.

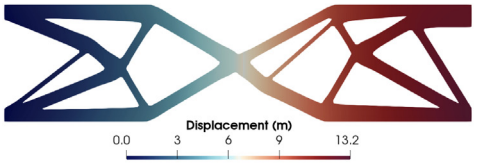

(A) $\nu_s = 0.4$. Displacement field (m)

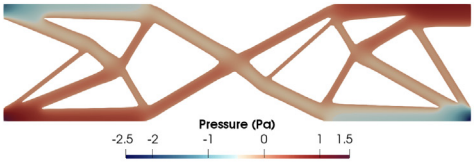

(B) $\nu_s = 0.4$. Pressure field (Pa)

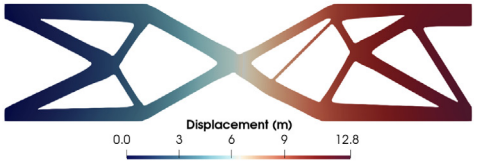

(C) $\nu_s = 0.45$. Displacement field (m)

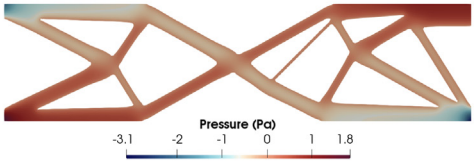

(D) $\nu_s = 0.45$. Pressure field (Pa)

Fig. 6. Single-point load beam. Final optimized structure in plane strain scenario for compressible materials with $\mathbf{u}/p/\mathbf{e}$ formulation.

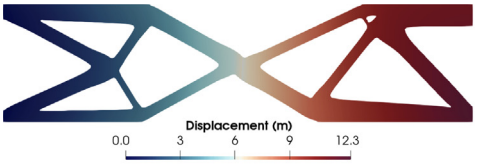

(A) $\mathbf{u}/p$ formulation. Displacement field (m)

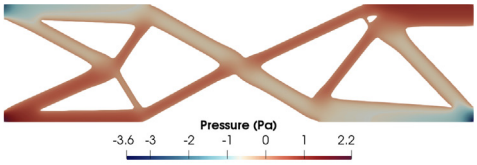

(B) $\mathbf{u}/p$ formulation. Pressure field (Pa)

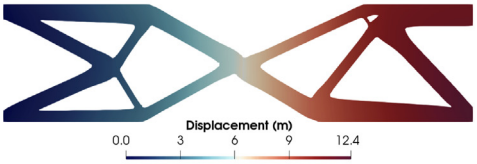

(C) $\mathbf{u}/p/\mathbf{e}$ formulation. Displacement field (m)

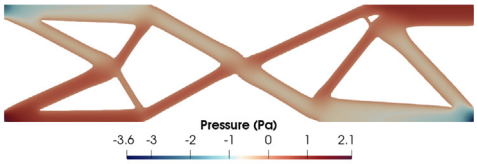

(D) $\mathbf{u}/p/\mathbf{e}$ formulation. Pressure field (Pa)

Fig. 7. Single-point load beam. Final optimized structure in plane strain scenario for $\nu_s = 0.5$ for both $\mathbf{u}/p$ and $\mathbf{u}/p/\mathbf{e}$ formulations.

Fig. 7 presents the results obtained for both mixed formulations when dealing with a fully incompressible strong material. The obtained design for incompressible material is quite different to the one presented in compressible scenarios. This structure appears to be made of less, yet thicker, structural elements.

The minor differences that can be noticed between formulations are caused by the different ways of computing the strains. In the $\mathbf{u}/p$ formulation the strains are computed from the displacement field, whereas, in the $\mathbf{u}/p/\mathbf{e}$ formulation, they are directly obtained as a nodal unknown.

Moving on to convergence issues, Fig. 8 shows a diagram referring to the compliance evolution recorded during the iterative topology optimization procedure, that leads to the designs shown in Fig. 7. A maximum of 100 iterations is imposed as stopping criteria to show the evolution of the objective functional. Both formulations need less than 100 iterations to minimize the compliance and achieve convergence.

5.2. Bearing device

As a second example, the topology optimization of a bearing device is explored. Since such devices are usually made of rubber we only consider the incompressible case. The geometry consists of a rectangular panel, clamped in the bottom side and subjected to a load distribution on the upper edge, t = 1.80 N/m. Stress free boundary conditions are applied on the remaining boundaries. We consider a linear elastic material with a Young Modulus $E_s = 100$ Pa. The geometry of this problem is shown in Fig. 9.

Exploiting the symmetry of the structure, only the left half of the original domain has been discretized, using about 19,200 linear triangular elements. The required final volume is set to be 35% of the domain. The study is conducted using the $\mathbf{u}/p$ formulation.

Fig. 10 shows the optimal structure obtained by using strong and weak materials, which are both incompressible. Because of the incompressibility of the weak material we obtain an extended zone of weak material elements,

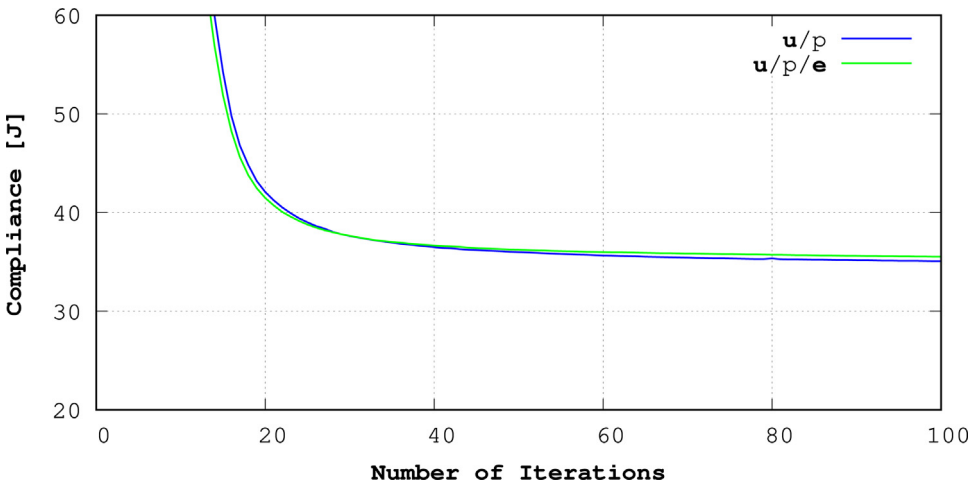

Fig. 8. Single-point load beam. Convergence diagrams in plane strain scenario for $\nu_s = 0.5$ for both $\mathbf{u}/p$ and $\mathbf{u}/p/\mathbf{e}$ formulations.

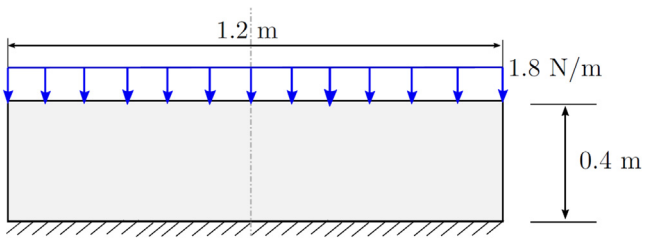

Fig. 9. Bearing device. Geometry.

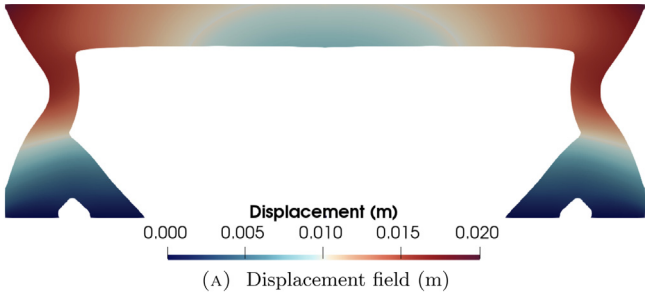

(A) Displacement field (m)

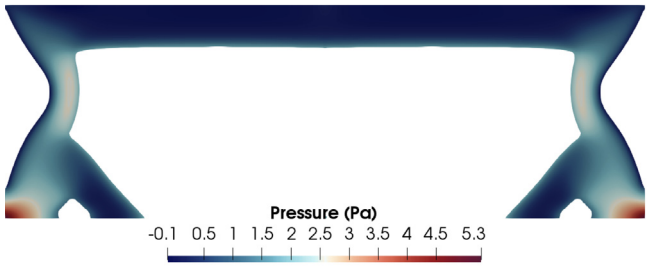

(B) Pressure field (Pa)

Fig. 10. Bearing device. Final optimized structure in plane strain scenario for $\nu_s = 0.5$ and $\nu_w = 0.5$ for $\mathbf{u}/p$ formulation.

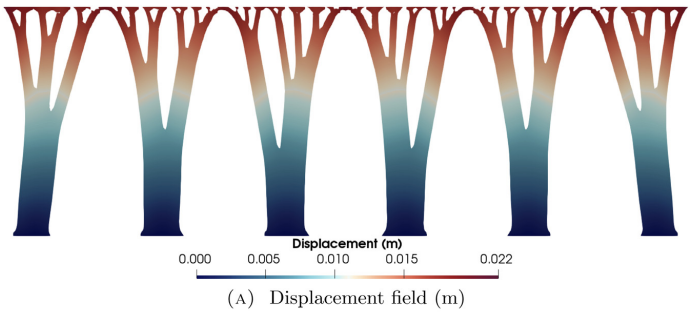

(A) Displacement field (m)

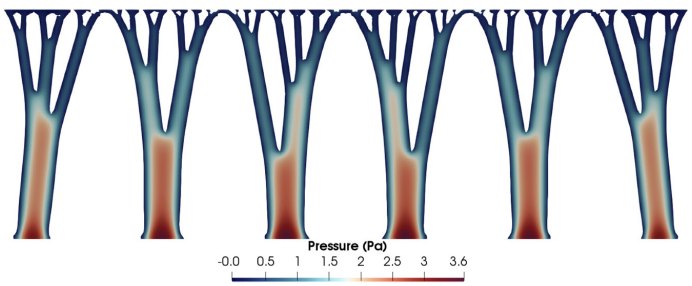

(B) Pressure field (Pa)

Fig. 11. Bearing device. Final optimized structure in plane strain scenario for $\nu_s = 0.5$ and $\nu_w = 0.4$ for $\mathbf{u}/p$ formulation.

enclosed by a structure made of strong material, as outlined in a similar example in [27]. To avoid this kind of designs, the weak material must be considered compressible, for example with $\nu_w = 0.4$. Fig. 11 illustrates the optimal topology which is obtained when this is taken into account. By considering a compressible weak material, widespread areas of elements made of weak material are not able to transfer the external pressure to the supports.

For the sake of completeness, Fig. 12 shows the evolution of the compliance along iterations for the previous two considerations of the weak material. A maximum of 40 iterations is imposed as stopping criteria. In the fully incompressible case, the widespread area of weak material is able to transfer the external pressure to the constraints,

which results in a very low compliance. This is the reason why the algorithm tends to this kind of 'optimal' design, where the compliance is even lower than the one obtained with a compressible weak material consideration.

It becomes evident, that weak material – if considered incompressible – can heavily contribute to the stiffness of the final structure, a behavior which goes against our assumption that the weak material is simulating void regions.

5.3. L-shaped beam

The third example is an L-shaped beam, a commonly exhibited problem in topology optimization. The specific feature of this problem is the geometrical singularity. The structure is clamped at the top and a single point force is applied at the middle of the right edge. Stress free boundary conditions are applied on the remaining boundaries. A linear elastic material is set with a Young Modulus $E_s = 1$ MPa. The geometry of this beam is shown in Fig. 13.

The domain has been discretized using roughly 22,800 linear triangular elements. The objective of this problem is to highlight the main differences between the mixed formulations proposed in this work. The required final volume is set to be 50% of the initial domain.

By using the deviatoric strains as an additional primary unknown in the $\mathbf{u}/p/\mathbf{e}$ formulation, the whole solution converges faster (upon h-refinement). Therefore, also the pressure and displacement fields are more accurate. This

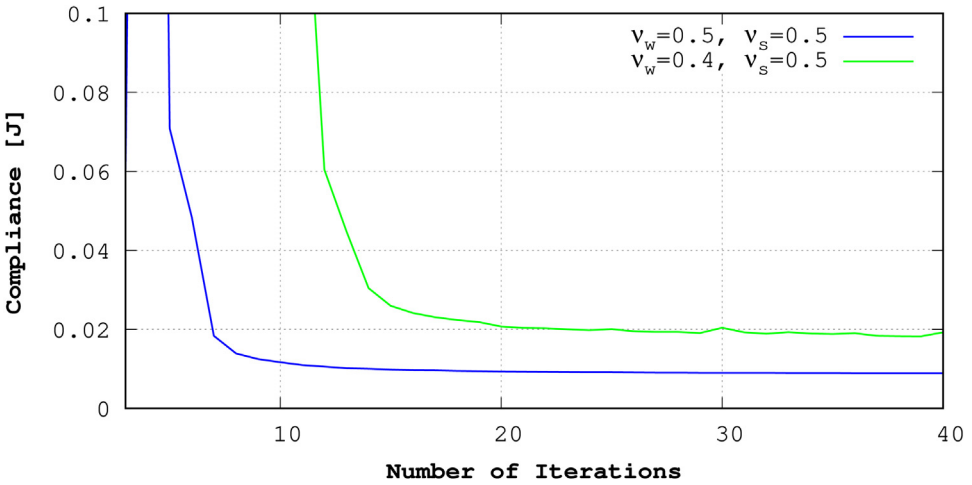

Fig. 12. Bearing device. Convergence diagrams in plane strain scenario for $\mathbf{u}/p$ formulation considering both $\nu_w = 0.4$ and $\nu_w = 0.5$.

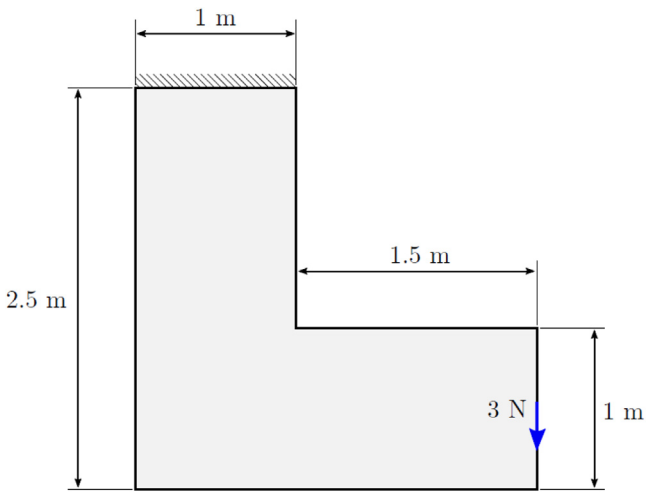

Fig. 13. L-shaped beam. Geometry.

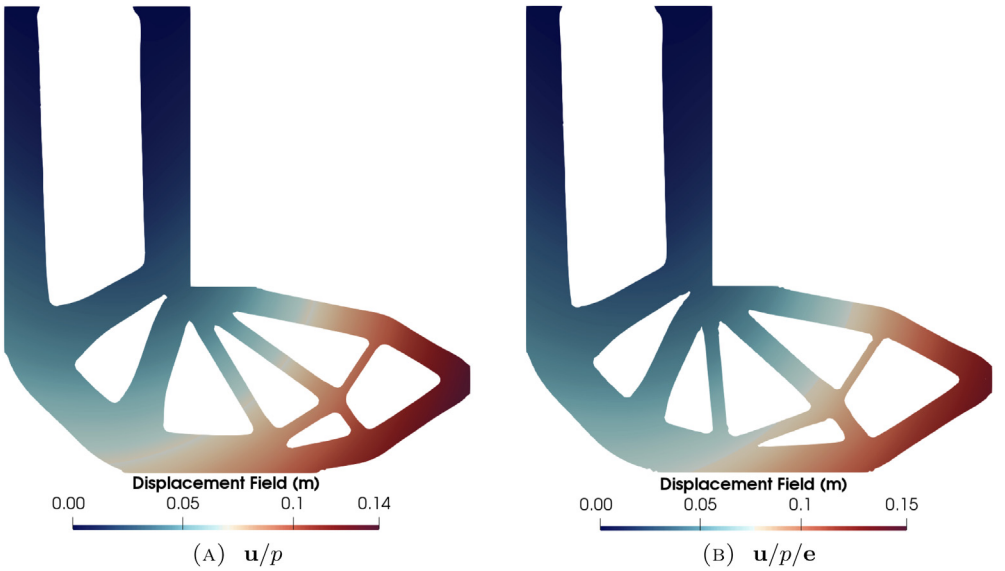

Fig. 14. L-shaped beam. Displacement field for the optimized structure for $\nu_s = 0.5$.

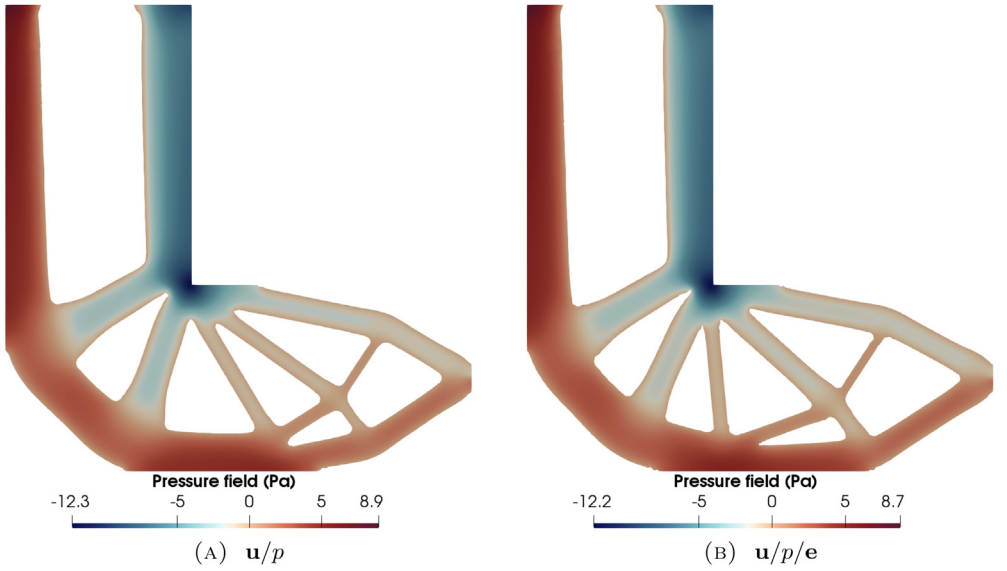

Fig. 15. L-shaped beam. Pressure field for the optimized structure for $\nu_s = 0.5$.

effect, however, is more dominant on coarser meshes. Due to the relatively fine discretization of our problem, we can only observe slight differences between the displacement and pressure fields of Figs. 14–15 in the final design of the optimized topology.

On the contrary, Fig. 16 shows the deviatoric strain field, obtained from both formulations. Utilizing the $\mathbf{u}/p$ formulation, the strains are computed from the displacement gradient and therefore defined element-wise. Because, linear triangular elements were used, the strains are element-wise constant, hence particularly imprecise. Using the $\mathbf{u}/p/\mathbf{e}$ formulation however, the deviatoric strains are also a primary unknown of the problem, and therefore defined at the nodes. The result is a continuous field, which is more precise in the first place and, secondly, does not require nodal smoothing for postprocessing. As a consequence the accuracy of the stresses is also increased.

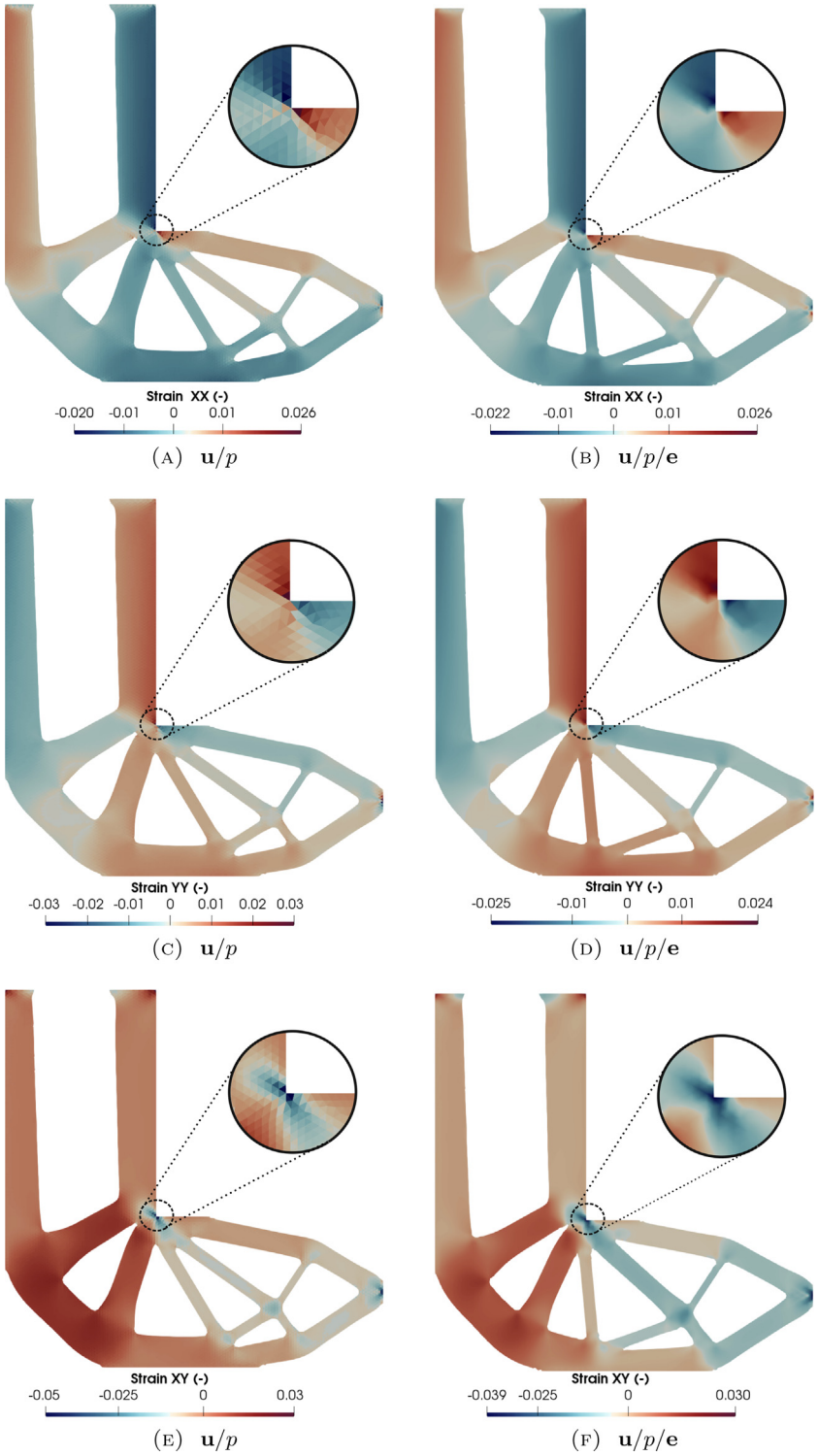

Fig. 16. L-shaped beam. Deviatoric strain field for the optimized structure for $\nu_s = 0.5$.

Remark 5.1. This extra level of accuracy in stresses and strains can be very interesting for several problems, such as Fluid–Structure Interaction or stress-constraint problems, among others. Note, however, that the rate of convergence of stresses and strains is expected to be the same for both the $\mathbf{u}/p$ and the $\mathbf{u}/p/\mathbf{e}$ formulations.

5.4. A 3D problem

The final example is a 3D Cantilever beam. The structure is clamped at the left face and a uniform traction is applied at the lower edge of the right face. Stress free boundary conditions are applied on the remaining boundaries. A linear elastic material is applied with a Young Modulus $E_s = 1$ MPa. The geometry of this beam is shown in Fig. 17.

Taking into account the symmetry of the problem, the left half of the design domain is discretized into 380,000 linear tetrahedral finite elements. The required final volume is set to be 10% of the initial one. Figs. 18–19 show the displacement and pressure fields for both formulations.

Fig. 20 presents the $L^2(\Omega)$-norm of the deviatoric strain field (Strain Magnitude) for each formulation. Again, a higher level of accuracy is obtained for the strains computed from the mixed $\mathbf{u}/p/\mathbf{e}$ formulation. The optimized structures are identical. The results of this problem indicate that it is reasonable to approximate the proper 3D polarization tensor with its isotropic 2D plane strain counterpart.

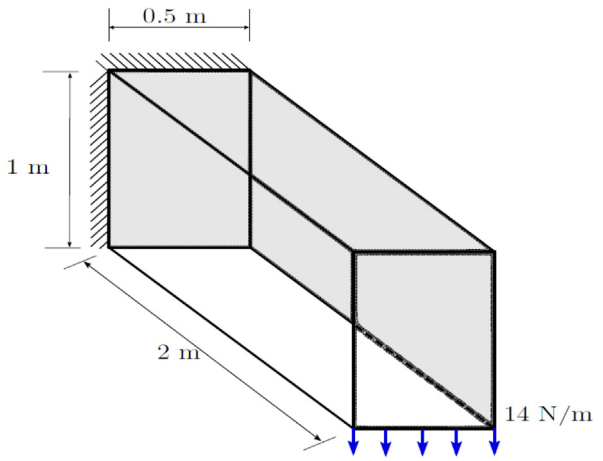

Fig. 17. 3D Cantilever beam. Geometry.

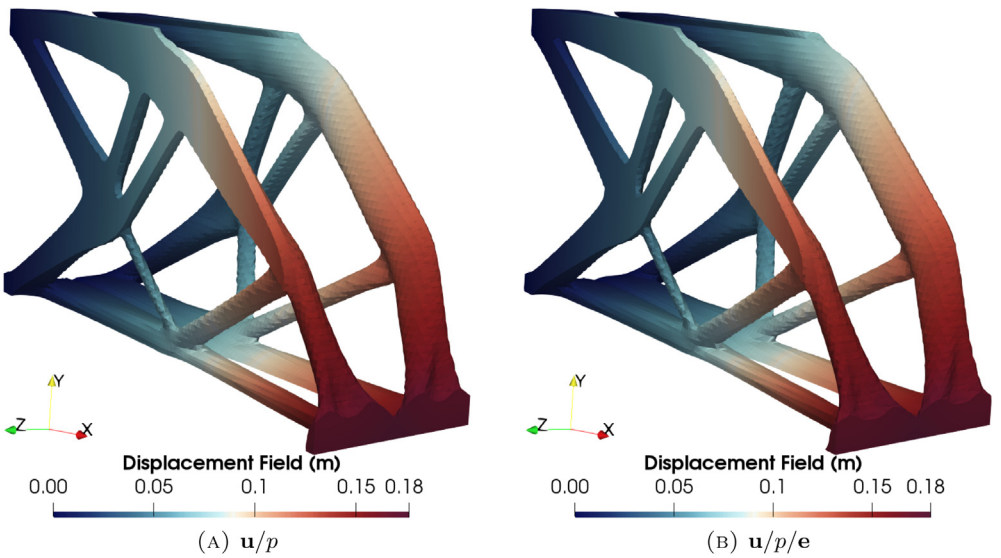

(A) $\mathbf{u}/p$ (B) $\mathbf{u}/p/\mathbf{e}$

Fig. 18. 3D Cantilever beam. Displacement field for the optimized structure in a 3D scenario for $\nu_s = 0.5$.

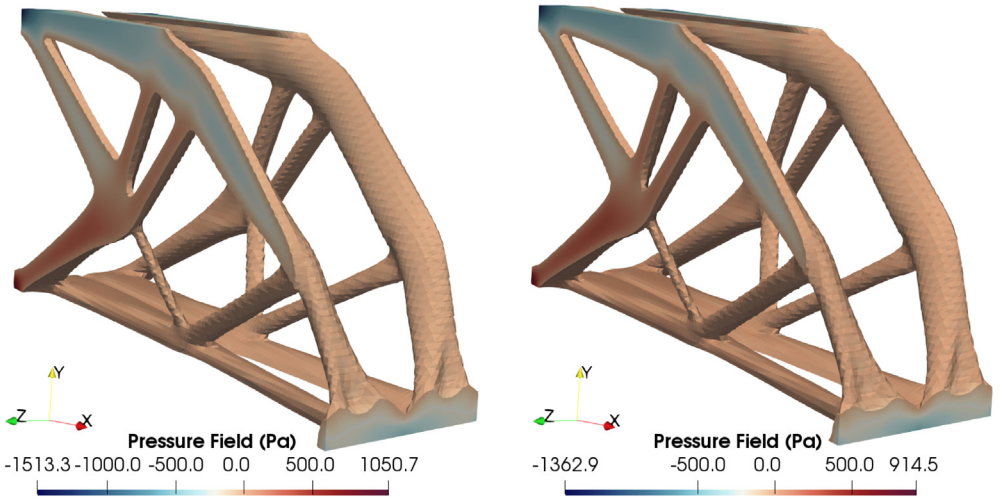

(A) $\mathbf{u}/p$ (B) $\mathbf{u}/p/\mathbf{e}$

Fig. 19. 3D Cantilever beam. Pressure field for the optimized structure in a 3D scenario for $\nu_s = 0.5$.

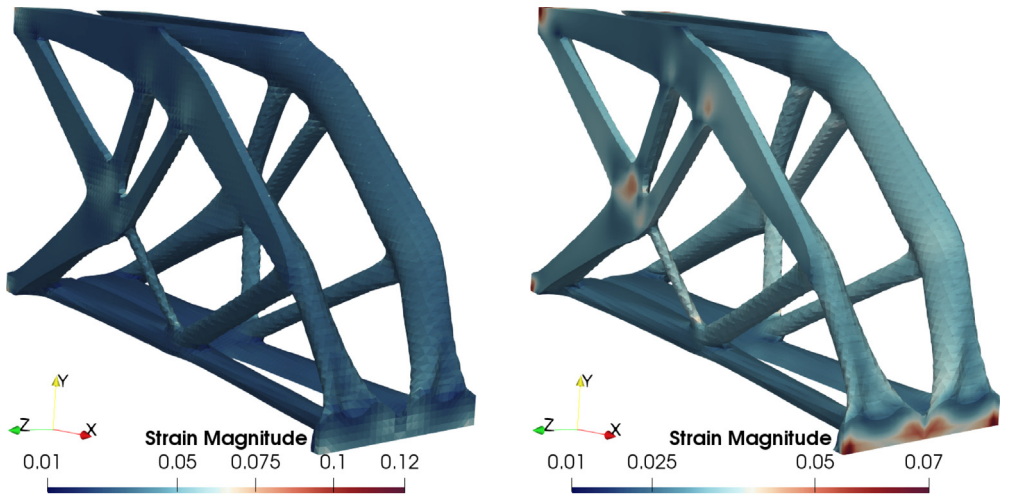

(A) $\mathbf{u}/p$ (B) $\mathbf{u}/p/\mathbf{e}$

Fig. 20. 3D Cantilever beam. Deviatoric strain field magnitude for the optimized structure in a 3D scenario for $\nu_s = 0.5$.

6. Conclusions

In this paper we have proposed a new method for handling topology optimization problems based on the topological derivative concept for nearly and fully incompressible materials. Departing from the splitting of the Polarization tensor into its deviatoric and spherical components, a new and simple expression for the topological derivative has been found. With this formulation, the study of linear elasticity topology optimization problems – while dealing with incompressible materials – is now possible.

The key to solving problems involving incompressibility was the introduction of two mixed stabilized finite element formulations in Section 2. On one hand, the well-known $\mathbf{u}/p$ formulation, in which the pressure is added as an unknown — the fundamental one, when dealing with incompressible materials. On the other hand, a relatively new three-field formulation $\mathbf{u}/p/\mathbf{e}$ which also adds the deviatoric strains as an unknown. In this setting, extra accuracy – particularly for strains and stresses – is obtained. This is due to the strains being no longer computed

through the symmetric gradient of the displacement but directly as nodal unknowns. The computation of the topological derivative benefits directly from this extra accuracy, since it depends directly on strains and stresses as shown in Section 3.

Thanks to the volumetric/deviatoric splitting, we have obtained two components for the Polarization tensor, one for computing the changes of the compliance shape functional caused by deviatoric effects and one for changes caused by volumetric effects. When the incompressible limit is reached, the former one presents no singularities, since it is being computed through both the deviatoric strains $\mathbf{e}$ and deviatoric stresses $\mathbf{s}$. The latter one depends on the pressure p and is formulated in terms of the bulk modulus κ to avoid singularities.

Regarding the topology optimization algorithm, presented in Section 4, we have developed an iterative computation scheme for the topological derivative. This was coupled with a level set strategy for the definition of the stiff and soft materials, which allows to keep a sharp track of the interface.

In Section 5 several numerical examples have been shown to assess the performance of the new split topological derivative expression. As presented in example 5.1, our formulation can automatically deal with the topology optimization of structures regardless the incompressibility of the given material. In example 5.2 we have shown the effects of considering an incompressible weak material and explained why this leads to undesired designs. Next, in example 5.3 we have presented the main differences between the $\mathbf{u}/p$ and the $\mathbf{u}/p/\mathbf{e}$ formulations with respect to the accuracy obtained for the main unknowns of the mechanical problem. Finally, example 5.4 was shown to demonstrate the good performance of our implementation in a 3D problem.

Declaration of competing interest

The authors declare that they have no known competing financial interests or personal relationships that could have appeared to influence the work reported in this paper.

Acknowledgments

I. Castañar gratefully acknowledges the support received from the Agència de Gestió d'Ajut i de Recerca through the predoctoral FI grant 2019-FI-B-00649. J. Baiges gratefully acknowledges the support of the Spanish Government through the Ramón *y* Cajal grant RYC-2015-17367. R. Codina gratefully acknowledges the support received through the ICREA Acadèmia Research Program of the Catalan Government, Spain. This work was partially funded through the TOP-FSI, Spain: RTI2018-098276-B-I00 project of the Spanish Government. CIMNE is a recipient of a "Severo Ochoa Programme for Centers of Excellence in R&D" grant (CEX2018-000797-S) by the Spanish Ministry of Economy and Competitiveness.

References

[1] M.P. Bendsøe, O. Sigmund, Topological Optimization: Theory, Springer, 2013.
[2] M.P. Bendsøe, N. Kikuchi, Generating optimal topologies in structural design using a homogenization method, Comput. Methods Appl. Mech. Engrg. 71 (2) (1988) 197–224.
[3] X. Huang, Y. Xie, A further review of ESO type methods for topology optimization, Struct. Multidiscip. Optim. 41 (2010) 671–683.
[4] N.P. van Dijk, K. Maute, M. Langelaar, F. van Keulen, Level-set methods for structural topology optimization: a review, Struct. Multidiscip. Optim. 48 (2013) 437–472.
[5] J.D. Deaton, R.V. Grandhi, A survey of structural and multidisciplinary continuum topology optimization: post 2000, Struct. Multidiscip. Optim. 49 (2014) 1–38.
[6] A.A. Novotny, J. Sokolowski, Topological Derivatives in Shape Optimization, Springer, 2013.
[7] Samuel Amstutz, Heiko Andrä, A new algorithm for topology optimization using a level-set method, J. Comput. Phys. 216 (2) (2006) 573–588.
[8] J. Baiges, J. Martí nez Frutos, D. Herrero-Pérez, F. Otero, A. Ferrer, Large-scale stochastic topology optimization using adaptive mesh refinement and coarsening through a two-level parallelization scheme, Comput. Methods Appl. Mech. Engrg. 343 (2019) 186–206.
[9] A.A. Novotny, J. Sokolowski, A. Zochowski, Topological derivatives of shape functionals. Part I: Theory in singularly perturbed geometrical domains, J. Optim. Theory Appl. 180 (2019) 341–373.
[10] J. Oliver, D. Yago, J. Cante, O. Lloberas-Valls, Variational approach to relaxed topological optimization: Closed form solutions for structural problems in a sequential pseudo-time framework, Comput. Methods Appl. Mech. Engrg. 355 (2019) 779–819.
[11] L.R.G. Treloar, The Physics of Rubber Elasticity, Oxford University Press, Oxford, NY, 1975.
[12] X. Oliver, C.A. de Saracibar, Continuum Mechanics for Engineers. Theory and Problems, 2nd Edition, 2017.
[13] T.J.R. Hughes, The Finite Element Method: Linear Static and Dynamic Finite Element Analysis, Prentice-Hall,Englewood Cliffs, New Jersey, 1987.

[14] T.J.R. Hughes, L.P. Franca, M. Balestra, A new finite element formulation for computational fluid dynamics: Circumventing the babuška-brezzi condition: a stable Petrov-Galerkin formulation of the Stokes problem accommodating equal-order interpolations, Comput. Methods Appl. Mech. Engrg. 59 (1986) 85–99.
[15] R. Codina, A stabilized finite element method for generalized stationary incompressible flows, Comput. Methods Appl. Mech. Engrg. 190 (2001) 2681–2706.
[16] L.P. Franca, T.J.R. Hughes, A.F.D. Loula, I. Miranda, A new family of stable elements for nearly incompressible elasticity based on a mixed Petrov-Galerkin finite element formulation, Numer. Math. 53 (1–2) (1988) 123–141.
[17] M. Chiumenti, Q. Valverde, C.A. de Saracibar, M. Cervera, A stabilized formulation for incompressible elasticity using linear displacement and pressure interpolations, Comput. Methods Appl. Mech. Engrg. 191 (2002) 1095–1116.
[18] M. Cervera, M. Chiumenti, R. Codina, Mixed stabilized finite element methods in nonlinear solid mechanics. Part I: Formulation, Comput. Methods Appl. Mech. Engrg. 199 (37–40) (2010) 2559–2570.
[19] M. Cervera, M. Chiumenti, R. Codina, Mixed stabilized finite element methods in nonlinear solid mechanics. Part II: Strain localization, Comput. Methods Appl. Mech. Engrg. 199 (37–40) (2010) 2571–2589.
[20] I. Castañar, J. Baiges, R. Codina, A stabilized mixed finite element approximation for incompressible finite strain solid dynamics using a total Lagrangian formulation, Comput. Methods Appl. Mech. Engrg. 368 (2020) 113164.
[21] R. Codina, Stabilization of incompressibility and convection through orthogonal sub-scales in finite element methods, Comput. Methods Appl. Mech. Engrg. 190 (2000) 1579–1599.
[22] R. Codina, Stabilized finite element approximation of transient incompressible flows using orthogonal subscales, Comput. Methods Appl. Mech. Engrg. 191 (2002) 4295–4321.
[23] T.J.R. Hughes, G.R. Feijóo, L. Mazzei, J. Quincy, The variational multiscale method - a paradigm for computational mechanics, Comput. Methods Appl. Mech. Engrg. 166 (1998) 3–24.
[24] M. Chiumenti, M. Cervera, R. Codina, A mixed three-field FE formulation for stress accurate analysis including the incompressible limit, Comput. Methods Appl. Mech. Engrg. 283 (2015) 1095–1116.
[25] R. Codina, Finite element approximation of the three field formulation of the Stokes problem using arbitrary interpolations, SIAM J. Numer. Anal. 47 (2009) 699–718.
[26] O. Sigmund, P.M. Clausen, Topology optimization using a mixed formulation: An alternative way to solve pressure load problems, Comput. Methods Appl. Mech. Engrg. 196 (2007) 1874–1889.
[27] M. Bruggi, P. Venini, Topology optimization of incompressible media using mixed finite elements, Comput. Methods Appl. Mech. Engrg. 196 (2007) 3151–3164.
[28] M. Stolpe, K. Svanberg, An alternative interpolation scheme for minimum compliance optimization, Struct. Multidiscip. Optim. 22 (2) (2001) 116–124.
[29] K. Svanberg, The method of moving asymptotes-a new method for minimum compliance optimization, Internat. J. Numer. Methods Engrg. 24 (1987) 359–373.
[30] C. Li, L. Tong, Topology optimization of incompressible materials based on the mixed SBFEM, Comput. Struct. 165 (2016) 24–33.
[31] G. Zhang, R. Alberdi, K. Khandelwal, Topology optimization with incompressible materials under small and finite deformations using mixed u/p elements, Internat. J. Numer. Methods Engrg. 115 (2018) 1015–1052.
[32] A.A. Novotny, J. Sokolowski, A. Zochowski, Topological derivatives of shape functionals. Part II: First-order method and applications, J. Optim. Theory Appl. 180 (2019) 683–710.
[33] I. Babuška, Error-bounds for finite element method, Numer. Math. 16 (4) (1971) 322–333.
[34] R. Codina, S. Badia, J. Baiges, J. Principe, Variational Multiscale Methods in Computational Fluid Dynamics, John Wiley & Sons Ltd., 2017.
[35] M. Chiumenti, M. Cervera, C.A. Moreira, G.B. Barbat, Stress, strain and dissipation accurate 3-field formulation for inelastic isochoric deformation, Finite Elem. Anal. Des. 192 (2021) 103534.
[36] A. Ferrer, SIMP-ALL: A generalized SIMP method based on the topological derivative concept, Internat. J. Numer. Methods Engrg. 120 (3) (2019) 361–381.
[37] M.P. Bendsøe, O. Sigmund, Material interpolation schemes in topology optimization, Arch. Appl. Mech. 69 (1999) 635–654.
[38] S.M. Giusti, A. Ferrer, J. Oliver, Topological sensitivity analysis in heterogeneous anisotropic elasticity problem. Theoretical and computational aspects, Comput. Methods Appl. Mech. Engrg. 311 (2016) 134–150.
[39] J.D. Eshelby, The determination of the elastic field of an ellipsoidal inclusion, and related problems, Proc. R. Soc.: Sect. A 241 (1957) 376–396.
[40] J.D. Eshelby, The elastic field outside an ellipsoidal inclusion, and related problems, Proc. R. Soc.: Sect. A 252 (1959) 561–569.
[41] C.G. Lopes, R. Batista dos Santos, A.A. Novotny, Topological derivative-based topology optimization of structures subject to multiple load-cases, Latin Amer. J. Solids Struct. 12 (2015) 834–860.
[42] Samuel Amstutz, Charles Dapogny, Àlex Ferrer, A consistent relaxation of optimal design problems for coupling shape and topological derivatives, Numer. Math. 140 (1) (2018) 35–94.
[43] S. Amstutz, S.M. Giusti, A.A. Novotny, E.A. De Souza Neto, Topological derivative for multi-scale linear elasticity models applied to the synthesis of microstructures, Internat. J. Numer. Methods Engrg. 84 (6) (2010) 733–756.
[44] M. Kishida, T. Kurahashi, J. Baiges, Application of a weighted sensitivity approach for topology optimization analysis of time dependent problems based on the density method, Japan Soc. Indust. Appl. Math. Lett. 13 (2021) 68–71.
[45] P.R. Amestoy, I.S. Duff, J. Koster, J.-Y. L'Excellent, A fully asynchronous multifrontal solver using distributed dynamic scheduling, SIAM J. Matrix Anal. Appl. 23 (1) (2001) 15–41.
[46] P.R. Amestoy, A. Buttari, J.-Y. L'Excellent, T. Mary, Performance and scalability of the block low-rank multifrontal factorization on multicore architectures, ACM Trans. Math. Software 45 (2019) 2:1–2:26.

[47] S. Balay, S. Abhyankar, M.F. Adams, J. Brown, P. Brune, K. Buschelman, L. Dalcin, V. Eijkhout, W.D. Gropp, D. Kaushik, M.G. Knepley, D.A. May, L. Curfman McInnes, R.T. Mills, T. Munson, K. Rupp, P. Sanan, B.F. Smith, S. Zampini, H. Zhang, H. Zhang, PETSc web page, 2015, http://www.mcs.anl.gov/petsc.